International Journal for Numerical Methods in Biomedical Engineering

WILEY

APPLIED RESEARCH

Modelling the Squishy Effect in Interstitial Pulmonary Fibrosis

Raffaella Rizzoni[1] | Roberto Tonelli[2] | Alessandro Marchioni[2]

[1]Department of Engineering, University of Ferrara, Ferrara, Italy | [2]University Hospital of Modena, Respiratory Diseases Unit, Department of Medical and Surgical Sciences, University of Modena Reggio Emilia, Modena, Italy

Correspondence: Raffaella Rizzoni (raffaella.rizzoni@unife.it)

Received: 27 May 2025 | **Revised:** 7 October 2025 | **Accepted:** 30 November 2025

Keywords: arbitrary polynomial chaos expansion | finite element method | global sensitivity analysis | idiopathic pulmonary fibrosis | non-linear elastic membrane | tension effects | ventilator-induced lung injury

ABSTRACT

In idiopathic pulmonary fibrosis (IPF), the juxtaposition of preserved regions and fibrotic areas creates heterogeneous lung mechanics and abnormal stress environments, which are hypothesized to activate mechanotransduction pathways and drive fibrosis progression. This study uses the "squishy ball lung" concept to quantify the potentially injurious mechanical stimuli arising from this heterogeneity. We developed a mechanical model that simulates the static inflation of an alveolus. This is described as a hyperelastic membrane with surface tension that is partially confined by springs representing fibrotic tissue. Finite element analysis (FEA) was used to assess the mechanical state under various confinement conditions. FEA revealed bulging deformation and significant meridian stress/strain peaks at transitions between confined and unconfined zones, which could potentially exceed safe physiological limits. To rigorously evaluate the predicted stress and strain environment, as well as its sensitivity to parameter uncertainty, such as material properties and the extent of confinement, we performed comprehensive uncertainty quantification (UQ) and quantitative sensitivity analysis (QSA). UQ confirmed the robustness of these localized stress peaks across parameter variations, while QSA identified the angle of confinement and spring stiffness as the primary determinants of peak stress magnitude. By quantifying these potentially injurious stress peaks, this study provides insights into the mechanical environment hypothesized to initiate mechanotransduction pathways in idiopathic pulmonary fibrosis (IPF), laying the groundwork for future studies that incorporate biological responses such as growth and remodeling.

1 | Introduction

Cellular mechanotransduction is a complex process by which mechanical stimuli are converted into biological responses through the activation of intracellular pathways [1]. This mechanism plays a critical role in various pathophysiological processes, including tissue repair, embryonic development, tumorigenesis, neural regeneration, and the progression of tissue fibrosis [2]. In lung physiology, mechanotransduction is essential for maintaining tissue homeostasis, as it regulates cellular responses to the mechanical forces exerted during breathing [3]. A key player in this process is the extracellular matrix (ECM), which not only provides structural support but also transmits mechanical signals to lung cells [4]. Cells such as alveolar epithelial cells, fibroblasts, and endothelial cells rely on their interaction with the ECM to sense and respond to the cyclic stretch and strain generated by normal respiratory dynamics [5]. The ECM's role extends beyond its function as a scaffold; it modulates the biomechanical environment, shaping how cells perceive and react to mechanical stimuli. By activating intracellular signaling pathways via mechanotransduction, lung tissue adapts to mechanical forces, enabling repair and regeneration while preventing maladaptive responses that could impair lung function [6].

In diseases such as IPF, however, this delicate balance is disrupted. IPF, a chronic, fibrosing interstitial pneumonia of unknown origin, is characterized by progressive loss of lung function, ultimately leading to respiratory failure and death [7]. The radiological and histological hallmark of IPF is the usual interstitial pneumonia (UIP) pattern, which features uneven fibrosis primarily affecting the lower lobes, with subpleural accentuation. Regions of preserved lung elasticity are juxtaposed to stiffer areas of inelastic fibrosis [8]. This patchy ECM stiffness alters respiratory mechanics, exposing the lung to abnormal mechanical stresses during both spontaneous breathing and mechanical ventilation (MV). These non-physiological forces may cause further damage to the lungs and dysregulate mechanotransduction pathways, worsening tissue remodeling and accelerating fibrosis progression [9].

While the role of biochemical pathways has long been known [10, 11], growing evidence highlighted the critical importance of mechanical forces in the development and progression of pulmonary fibrosis, particularly in IPF. Substrate stiffness deeply affects fibroblast behavior, including collagen deposition and proliferation, establishing a basis for positive feedback in fibrosis [6, 12–16]. Further studies consolidated the role of cyclical stretch in the lungs, showing its impact on fibroblast behavior through mechanisms such as the activation of stretch-regulated channels [17, 18]. Crucially, stretch was also identified as a contributor to the release of latent TGF-β1, a cytokine essential for wound healing and myofibroblast differentiation [9, 15, 19, 20]. Furthermore, the identification of mechanosensitive signaling pathways like YAP (Yes-associated protein) and MRTF-A (Myocardin-related transcription factor A), transcriptional regulators linked to fibroblast proliferation and ECM deposition in response to cyclical stretch provided further understanding [6, 14, 15]. These findings converge to support the “mechanical vicious cycle” hypothesis in IPF, a well-established concept, with early proposals in [19] and references therein. According to this hypothesis, excessive collagen accumulation and remodeling by myofibroblasts cause ECM fibers to become denser and straighter. This results in higher overall tissue stiffness, which limits the lungs to full expand during breathing. Consequently, even small strains in the fibrotic tissue can generate substantial stresses, sufficient to trigger the release of active TGF-β1 from the ECM, causing fibroblasts to differentiate into myofibroblasts, which then further contribute to ECM deposition and remodeling, closing a self-sustaining, positive feedback chemo-mechanical loop.

During acute exacerbations of idiopathic pulmonary fibrosis (AE-IPF), the increased mechanical stress imposed on an already heterogeneous lung structure—either due to intensified spontaneous breathing [21] or ventilatory support—may lead to excessive tissue deformation during inflation. In this context, regions of preserved elasticity may bulge adjacent to stiff, fibrotic areas, an effect described by the “squishy ball lung” theory [22]. This theory likens the mechanical deformation of these lung regions to that of a stress ball, where localized stress exceeds the threshold needed to activate mechanotransduction pathways, further amplifying the damaging mechanotransduction pathways central to the “mechanical vicious cycle”. Consequently, the dysregulated mechanotransduction in IPF exacerbates the chronic and progressive nature of the disease, perpetuating a cycle of fibrosis and declining lung function. Furthermore, mechanical stress during spontaneous breathing is unevenly distributed, with the lower lobes experiencing the greatest stretch during inflation. This “squishy” behavior of the fibrotic lung may help explain why IPF tends to progress along the axis of mechanical force distribution over time [23].

Several numerical models investigating IPF have been documented in the literature, see [24] for a recent review. At the alveolar scale, Hall et al. have proposed a computational model combining individual cell behaviors (agent-based) with a simplified tissue structure (spring network) to study IPF [25]. The model shows that fibroblast responses to both ECM stiffness and stretch determine whether the tissue heals or becomes fibrotic, highlighting how the initial tissue damage structure and the balance of these mechanical signals can lead to disease progression and heterogeneous structures typical of IPF.

At the tissue scale, several continuum mechanics models [26, 27], constitutive approaches based on finite-deformation homogenization [28], and advanced poromechanical constitutive description [29, 30] have been proposed to characterize the regional lung deformation, airflow, and the impact of tissue remodeling on overall lung function. These models are crucial for predicting global responses and assessing the impact of diffuse disease patterns. Nevertheless, the bulk material properties and damage criteria used in these organ-scale simulations often average out the mechanical interplay occurring at the microscale, particularly within the heterogeneous environment of the fibrotic lung. The juxtaposition of stiff, fibrotic foci with more compliant, preserved alveolar structures in IPF creates local stress and strain fields that are difficult to resolve by larger-scale models but are hypothesized to be critical drivers of disease progression via mechanotransduction. Understanding the nature and quantifying magnitude of these micro-mechanical stimuli is therefore essential. Accordingly, the primary aim of our study is to present an alveolar model specifically designed to quantify stress and strain peaks arising from the heterogeneous nature of fibrotic tissue, simulating its non-linear elastic behavior during inflation at the microscale while accounting for the heterogeneous distribution of fibrotic tissue. In particular, the study investigates whether the deformation of an elastically heterogeneous structure, as seen in IPF, can account for a “squishy” behavior. To this end, the proposed model integrates a hyperelastic membrane representation of a single alveolus with an axisymmetric distribution of linear springs to simulate partial fibrotic confinement, as illustrated in Figure 1a,b. Notably, the multiscale nature of lung tissue makes it amenable to modeling approaches based on homogenization techniques for deriving its effective mechanical properties. One rigorous approach is two-scale asymptotic homogenization, which efficiently upscales the behavior of complex microstructures, such as linear and nonlinear poroelastic composites, without prior kinematic assumptions [31, 32]. As an alternative approach, we describe the single alveolus using a membrane model previously derived by an analytical homogenization and upscaling technique [33]. This technique reduces a three-dimensional, multilayered, composite, thick shell subjected to axially symmetric deformations

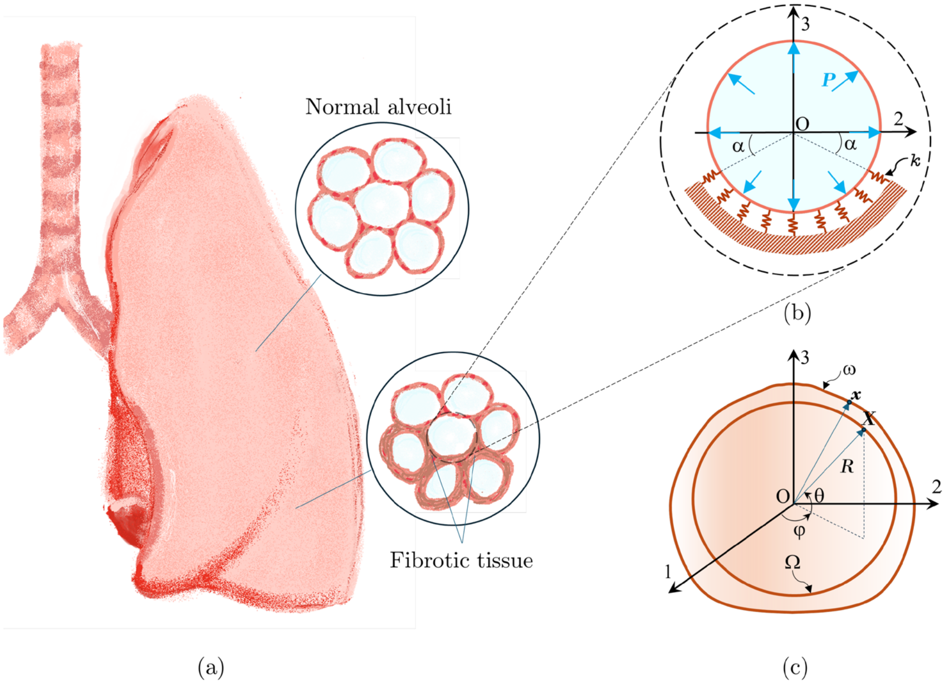

FIGURE 1 | (a) IPF leads to a heterogeneous distribution of normal-appearing lung regions adjacent to fibrotic tissue, characterized by increased stiffness. (b) Normal alveoli adjacent to fibrotic tissue are modeled as pressurized, nonlinearly hyperelastic membranes constrained by fibrotic lesions, which are represented as an elastic foundation (with stiffness k) partially enclosing the membrane. (c) Reference frameworks for the undeformed (Ω) and deformed (ω) axisymmetric configurations of the pressurized elastic membrane representing the alveolus.

to a computationally efficient membrane formulation. Although this analytical approach relies on axial symmetry, it results in a highly efficient computational membrane formulation. This efficiency is a critical advantage for the comprehensive uncertainty quantification and global sensitivity analysis presented here.

In Section 2.1, the equilibrium configurations of the alveolar membrane are assumed to minimize a potential energy functional (10) defined over axially symmetric configurations. The effect of surfactant is included through the surface tension model proposed by Kowe et al. [34]. The strain energy density, based on the approach described in [33], includes two contributions: one accounting for the elastic behavior of elastin fibers and the other accounting for the elasticity of collagen fibers. Additionally, a pressure loading potential is assumed to account for alveolar inflation.

For the two limiting cases of free inflation (the absence of springs) and full confinement (complete coverage of the membrane by springs), the corresponding energy minimizer for spherical inflation of the alveolar membrane can be determined analytically. This yields closed-form solutions for the strain and stress components.

For partial spring distributions around the alveolus, nonspherical configurations are expected at equilibrium. We use the FreeFEM software [35], based on the Finite Element Method, to compute these configurations. Section 3 provides details on the finite element implementation. The computational model developed in FreeFEM allows us to calculate the deformed configuration, as well as the strain and stress distributions at equilibrium in the meridian, circumferential, and radial directions of the alveolus. This numerical analysis enables us to identify regions that are likely to activate mechanotransduction pathways. The FEA numerical results are presented and discussed in Section 4.

To increase confidence in the predictions from our alveolar model, it is essential to account for the inherent uncertainties in its input parameters. These uncertainties arise from factors such as natural biological variation and the precision of experimental measurements. Consequently, we performed Uncertainty Quantification (UQ) to determine the range of stress and strain peaks given these parameter uncertainties. Alongside UQ, we performed Quantitative Sensitivity Analysis (SA) to determine the relative importance of each input parameter in driving the model's predictions. This highlighted the factors that most strongly influence the micro-mechanical environment. For UQ and SA, we employed an arbitrary polynomial chaos (aPC) expansion approach. This surrogate modeling technique was chosen for its computational efficiency in handling complex models and for its rigorous mathematical framework for propagating uncertainties and deriving sensitivity indices. The availability of robust open-source toolboxes, such as the *Data-driven Arbitrary Polynomial Chaos* MATLAB toolbox [36, 37], further facilitated its implementation. Details of its application to the alveolar model are provided in Section 5.

Unlike conventional alveolar models, our approach introduces a key novelty: the incorporation of heterogeneous fibrotic tissue distribution, a key feature of IPF. This departure from the idealized assumption of uniform alveolar elasticity provides a more realistic representation of fibrosis-induced mechanical alterations, as explained in Section 6.

Although membrane models for alveoli have already been proposed in the literature, to our knowledge this study is the first to employ an axisymmetric spring-confined hyperelastic membrane model to quantify stress and strain amplification specifically at the interface of preserved tissue and fibrotic regions. This provides a mechanical basis for the "squishy ball" hypothesis in IPF. Another novel element of this work is the comprehensive UQ and GSA performed. This rigorous approach enabled us to predict strain and stress peaks, assess the robustness of these predictions across variations in physiological parameters, and identify the geometric and material parameters most critical to these peaks.

2 | Materials and Methods

2.1 | Problem Formulation

In the model, a single alveolus is represented as a thin spherical membrane with radius R and an initial thickness $h = \epsilon R$, where $\epsilon < < 1$. The alveolus is inflated by a given internal pressure P. The position vector $\mathbf{X}$ defines the location of a particle in the initial, undeformed membrane configuration, Ω, while the position vector $\mathbf{x}$ defines the corresponding current position of the particle in the deformed membrane configuration ω, as shown in Figure 1c. Both position vectors, $\mathbf{X}$ and $\mathbf{x}$, are referred to a set of spherical coordinates (r, θ, ϕ), where r is the radial distance, θ is the elevation angle and ϕ is the azimuthal angle, as illustrated in Figure 1c.

The undeformed configuration of the membrane is given by $\Omega = S \times \{-h/2, h/2\}$, where S is the initial middle surface of the membrane, i.e., the sphere of radius R centered at the origin, described by the equations:

$$\begin{aligned} X_1 &= R\cos\phi\cos\theta, \\ X_2 &= R\sin\phi\cos\theta, \\ X_3 &= R\sin\theta, \end{aligned} \tag{1}$$

where $-\pi/2 \leq \theta \leq \pi/2$, $0 \leq \phi < 2\pi$. Under the assumption of axially symmetric deformations, the deformed configuration is $\omega = s \times \{-t/2, t/2\}$, where t is the deformed thickness, and s is the deformed middle surface, described by the equations:

$$\begin{aligned} x_1 &= R\ \xi(\theta)\cos\phi, \\ x_2 &= R\ \xi(\theta)\sin\phi, \\ x_3 &= R\ \zeta(\theta), \end{aligned} \tag{2}$$

where ξ and ζ are unknown functions of θ describing the normalized profile of the deformed configuration. To prevent rigid body motions, we assume

$$\xi(\pm\pi/2) = 0. \tag{3}$$

The meridional and circumferential strains, λ_θ and λ_ϕ, respectively, are

$$\lambda_\theta = \sqrt{\xi'^2(\theta) + \zeta'^2(\theta)}, \qquad \lambda_\phi = \frac{\xi(\theta)}{\cos\theta}, \tag{4}$$

and the strain ratio describing the change in thickness h at a generic point $\mathbf{X}$ during deformation is

$$\lambda_r = \frac{t}{\epsilon R}, \tag{5}$$

where t is the deformed thickness at $\mathbf{x}$.

The material composing the membrane is assumed to be nonlinear hyperelastic, homogeneous and incompressible, and described by a strain energy density $w(\lambda_\theta, \lambda_\phi, \lambda_r)$ which depends on λ_θ, λ_ϕ, and λ_r through the strain invariants. Due to incompressibility, the product of the strains is unitary:

$$\lambda_\theta\lambda_\phi\lambda_r = 1, \tag{6}$$

so that only λ_θ and λ_ϕ are independent, with λ_r being determined by the relation above. The incompressibility assumption is common for modeling soft biological tissues under physiological loading conditions, see for example [38]. Here, it was assumed for consistency with previous work that derived the material parameters used herein from fitting clinical data using an incompressible alveolar shell model [33].

Following the derivation of the membrane model for a single alveolus presented in our previous work [33], the strain energy density that models the elastic behavior of the material composing the alveolar membrane is written as follows:

$$w(\lambda_\theta, \lambda_\phi, \lambda_r) = c_1(1-\chi)\left(\lambda_\theta^2 + \lambda_\phi^2 + \lambda_r^2 - 3\right) + c_2\chi\left(\lambda_\theta^2 + \lambda_\phi^2 + \lambda_r^2 - 3\right)^3, \tag{7}$$

where c_1, c_2 are positive material parameters and $\chi \in (0, 1)$. The strain energy density (7) consists of two contributions: the first addend accounts for the elastic behavior of elastin fibers, while the second addend accounts for the elasticity of collagen fibers. At the alveolar level, these two types of fibers are interconnected within the complex tissue network. In this model, the coefficient χ represents the volume fraction of collagen fibers, while c_1 and c_2 are the elasticity constants for elastin and collagen fibers, respectively. In our previous work [33], Equation (7) was rigorously derived from the principles of finite elasticity, not assumed phenomenologically. The derivation begins with a three-dimensional multilayered composite thick shell. Through the analytical integration of the equilibrium equations across the layers, followed by an asymptotic expansion for a thin shell, the final membrane approximation is obtained, giving a governing pressure-volume relationship based on Equation (7). However, it is important to note that the theoretical and numerical framework presented here is independent of this specific choice and can accommodate other types of hyperelastic strain energy functions.

To model the presence of fibrotic tissue surrounding the alveolus, we introduce a continuous distribution of linear springs acting on a part of the external surface, taken to coincide with S, with the extent of the spring distribution determined by the angle $\alpha \in [-\pi/2, \pi/2]$, as depicted in Figure 1b. Where present, the elastic foundation is characterized by a uniform spring stiffness $k > 0$, which models the confining effect of fibrotic tissue surrounding the alveolus. We define the area fraction of surrounding fibrotic tissue, ϖ, as the ratio of the area of the undeformed surface onto which the springs are distributed, to the total area of S. Using the formula for the area of a spherical cap, the angle α is related to ϖ by the following equation:

$$\varpi = \frac{1}{2} + \frac{1}{2}\sin\alpha. \tag{8}$$

In the present model, we incorporate the effect of surface tension on the local mechanical response of alveolar tissue due to the presence of surfactant. This is a thin liquid film composed of a mixture of lipids and proteins secreted by alveolar cells in the lungs. We adopt the surface tension model (III) for inflation proposed by Kowe et al. in [34], which is based on the following exponential expression for the surface free energy Γ per unit area in the current configuration:

$$\Gamma\left(J_2\right) = \gamma\left(1 + \frac{d_1}{d_2 J_2} e^{-d_2 J_2}\right), \tag{9}$$

where $\gamma = 0.04$ N/m is the maximum surface tension, and d_1 and d_2 are constants taking values 10.0 and 2.35, respectively. J_2 represents the ratio of the area element in the current configuration to that in the reference configuration, with $J_2 = \lambda_\theta \lambda_\phi$.

Finally, the membrane supports a uniformly distributed inflation pressure P, see Figure 1b.

At equilibrium, the system occupies a configuration that is assumed to minimize the total potential energy, given by

$$\begin{aligned}\mathcal{E}(\xi,\zeta) = &\int_\Omega w\left(\lambda_\theta, \lambda_\phi, \lambda_r\right)\, dV + \int_S \lambda_\theta\lambda_\phi\Gamma\left(\lambda_\theta\lambda_\phi\right)dA \\ &+ \int_S \frac{1}{2}kR^2\left(\|\xi - \cos\theta\|^2 + \|\zeta - \sin\theta\|^2\right)dA - P\ vol(\omega),\end{aligned} \tag{10}$$

where $vol(\omega)$ is the volume enclosed by the deformed configuration ω. This volume can be calculated as

$$vol(\omega) = \frac{1}{3}\int_S \mathbf{x}\cdot\frac{\left(\mathbf{x}_{,1}\wedge\mathbf{x}_{,2}\right)}{\|\mathbf{X}_{,1}\wedge\mathbf{X}_{,2}\|}\ dA. \tag{11}$$

This volume functional gives a reasonable expression for the volume of the region enclosed by the deformed membrane configuration ω, see [39].

Using the assumption of axial symmetry (2) and the boundary conditions (3), minimizers of $\mathcal{E}$ also minimize the rescaled total potential energy:

$$\begin{aligned}\widetilde{\mathcal{E}}(\xi,\zeta) = &\int_{-\pi/2}^{\pi/2} \widetilde{w}\left(\lambda_\theta, \lambda_\phi, \lambda_r\right)\cos\theta\ d\theta + \int_{-\pi/2}^{\pi/2} \lambda_\theta\lambda_\phi\widetilde{\Gamma}\left(\lambda_\theta\lambda_\phi\right)\cos\theta\ d\theta \\ &+ \int_{-\pi/2}^{\pi/2} \frac{\widetilde{k}}{2}\left(\|\xi - \cos\theta\|^2 + \|\zeta - \sin\theta\|^2\right)\cos\theta\ d\theta - \frac{\widetilde{P}}{2}\int_{-\pi/2}^{\pi/2} \xi^2\zeta' d\theta,\end{aligned} \tag{12}$$

where

$$\begin{aligned}&\widetilde{w} := \frac{w}{c_1} = (1-\chi)\left(\lambda_\theta^2 + \lambda_\phi^2 + \lambda_r^2 - 3\right) + g\ \chi\left(\lambda_\theta^2 + \lambda_\phi^2 + \lambda_r^2 - 3\right)^3, \quad g := c_2/c_1, \\ &\widetilde{\Gamma} := \frac{\Gamma}{\epsilon\ c_1 R} = \widetilde{\gamma}\left(1 + \frac{d_1}{d_2\lambda_\theta\lambda_\phi}e^{-d_2\lambda_\theta\lambda_\phi}\right), \\ &\widetilde{\gamma} := \frac{\gamma}{\epsilon\ c_1 R}, \\ &\widetilde{k} := \frac{kR}{\epsilon\ c_1}, \\ &\widetilde{P} := \frac{P}{\epsilon\ c_1},\end{aligned}$$

represent the normalized elastic energy density, the ratio of collagen stiffness to elastin stiffness, the normalized surface free energy, the normalized spring stiffness function, and the normalized pressure, respectively.

Equilibrium configurations of the pressurized alveolus correspond to pairs (ξ, ζ) that minimize the energy $\mathcal{E}$ within the set:

$$V = \left\{(\xi,\zeta) \in W^{1,2}(I) \times W^{1,2}(I) \,|\, \xi(\pm\pi/2) = 0\right\}, \tag{13}$$

where $I = (-\pi/2, \pi/2)$.

To study the stress distribution in the membrane, we introduce the dimensionless stress components per unit length of the deformed elastic membrane, defined by:

$$\widetilde{\sigma}_i := \lambda_i \frac{\partial\widetilde{w}}{\partial\lambda_i} - \widetilde{p}, \tag{14}$$

for the radial ($i = r$), circumferential ($i = \phi$) and meridian ($i = \theta$) directions. In (14), $\widetilde{p}$ represents the normalized pressure reaction field due the incompressibility constraint. Using the boundary condition $\sigma_r = P$, with P the inflation pressure acting inside the membrane, $\widetilde{p}$ can be calculated as:

$$\widetilde{p} = \lambda_r \frac{\partial\widetilde{w}}{\partial\lambda_r} - \epsilon\widetilde{P}. \tag{15}$$

Substituting this into (14), we obtain the final form for the normalized stress components:

$$\widetilde{\sigma}_i = \left(\lambda_i^2 - \lambda_r^2\right)\left[2(1-\chi) + 6g\chi\left(\lambda_\theta^2 + \lambda_\phi^2 + \lambda_r^2 - 3\right)^2\right] + \epsilon\widetilde{P}, \tag{16}$$

for $i = \theta, \phi, r$.

Where present, the magnitude of the contact stress due to the spring distribution is

$$f_k = kR\ \sqrt{(\xi - \cos\theta)^2 + (\zeta - \sin\theta)^2}. \tag{17}$$

For $\alpha = \pi/2$, corresponding to a fully confined alveolus, the applied pressure is expected to induce spherical inflation of the membrane. Therefore, a minimizer of the rescaled energy (12) in V is sought in the form:

$$\xi_s(\theta) = \lambda_s\cos\theta, \qquad \zeta_s(\theta) = \lambda_s\sin\theta, \tag{18}$$

where λ_s is an unknown positive parameter representing the (meridional and circumferential) strain. Substituting these into the energy (12) yields the following expression for the energy in the case $\alpha = \pi/2$:

$$\widetilde{\mathcal{E}}(\xi_s, \zeta_s) = \; 2\widehat{w}(\lambda_s) + 2\widehat{\Gamma}(\lambda_s) + \widetilde{k}\;(\lambda_s - 1)^2 - \frac{2\widetilde{P}}{3}\lambda_s^3, \qquad (19)$$

where $\widehat{w}(\lambda_s) := \widetilde{w}(\lambda_s, \lambda_s, 1/\lambda_s^2)$ and $\widehat{\Gamma}(\lambda_s) := \lambda_s^2\, \widetilde{\Gamma}(\lambda_s^2)$. Minimizing the energy (19) with respect to λ_s gives:

$$\widetilde{P} = \frac{1}{\lambda_s^2}\frac{\partial \widehat{w}}{\partial \lambda_s} + \frac{1}{\lambda_s^2}\frac{\partial \widehat{\Gamma}}{\partial \lambda_s} + \widetilde{k}\frac{(\lambda_s - 1)}{\lambda_s^2}. \qquad (20)$$

Given the normalized pressure $\widetilde{P}$, the solution λ_s of Equation (20) provides the equilibrium value of λ_s for the case $\alpha = \pi/2$, corresponding to the deformation of an inflated alveolus fully confined by the surrounding fibrotic tissue.

For the case $\alpha = -\pi/2$, corresponding to an unconfined alveolus, the equilibrium configuration is sought in the same form as Equation (18), with λ_s now given by the solution to Equation (20) with $\widetilde{k} = 0$.

In both radially symmetric cases ($\alpha = \pm\pi/2$) the meridian and circumferential stress components are equal and uniform, i.e., independent of θ, and their value, σ_s, can still be computed using Equations (14) and (15) with $\lambda_\theta = \lambda_\phi = \lambda_s$, and λ_s calculated as described above.

For partial distributions of springs around the alveolus, with angles α such that $0 < \alpha < \pi/2$, non-spherical equilibrium configurations are expected. In the next section, we introduce a numerical procedure to calculate these configurations.

3 | Finite Element Implementation

To minimize the rescaled energy (12), we employed the FreeFEM software [35], which is based on the Finite Element Method [40]. The procedure followed aligns with the steps outlined in the FreeFEM documentation for solving nonlinear elasticity problems and utilizes the Newton–Raphson algorithm [41]. The interval I was represented as a rectangle with a small aspect ratio (1: 100). The minimizing functions ξ, ζ were approximated using piecewise linear continuous bidimensional finite elements ($P1$) defined on an initial triangulation of a 100×10 grid, further adapted using the *adaptmesh* function. The results were exported and visualized using MATLAB [42].

To check the numerical accuracy of the FEA model, a mesh convergence study was conducted prior to the UQ/GSA. For this study, all physical parameters were held constant using the values listed in Table 1. Parameters treated as uncertain in the subsequent UQ/GSA were set to their respective mean

TABLE 1 | Geometrical, material, loading, and uncertainty parameters used in the FEA and UQ/GSA.

Symbol	Description	Type	Value/parameters	Units
Fixed parameters				
ϵ	Thickness-to-radius ratio	Fixed	0.05[a]	[–]
R	Reference Radius	Fixed	1.1526×10^{-4}[b]	m
Loading parameters (scenarios)				
P	Applied Pressure	Scenario	{1.6, 3.2, 8.0, 16.0, 24.0, 32.0}	cmH_2O
Uncertain parameters (inputs for UQ/SA)				
c_1	Elastin elasticity parameter	Lognormal[c,e]	Mean = 53.24, SD = 6.93	cmH_2O
c_2	Collagen elasticity parameter	Lognormal[c,e]	Mean = 365.0, SD = 60.69	cmH_2O
χ	Collagen volume fraction	Uniform	Min = 0.05, Max = 0.29[d]	[–]
α	Angle of fibrotic tissue distribution	Uniform	Min = $-\pi/2$, Max = $\pi/2$[f]	rad
k	Spring (fibrotic tissue) stiffness	Uniform	Min = 509.85, Max = 1019.7[g]	cmH_2O
γ	Surface tension coefficient	Uniform[h]	Min = 3.26×10^{-4}, Max = 4.90×10^{-4}	cmH_2O m
d_1	Surfactant model parameter	Uniform[h]	Min = 8.0, Max = 12.0	[–]
d_2	Surfactant model parameter	Uniform[h]	Min = 1.88, Max = 2.82	[–]

[a] Value proposed by Jawde et al. [43].
[b] Value based on Equation (S3) in [43] for a body weight of 70 kg.
[c] Lognormal distribution parameters derived from Mean and 95% CI estimated; SD calculated assuming CI represents ± 1.96 × SD.
[d] Range selected based on physical considerations (minimum 5 % collagen in healthy tissue; upper bound from [33]), and to ensure numerical stability by avoiding near-zero collagen scenarios.
[e] Mean and CI values for c_1 and c_2 taken from previous work [33].
[f] Assumed uniform distribution for angle of fibrotic tissue distribution, representing heterogeneity.
[g] Range for spring stiffness based on an estimated stiffness variation of 50–100 kPa in highly fibrotic regions, cf. [44, 45].
[h] Derived assuming ± 20 % variation around the nominal values $\gamma = 0.04$ N/m, $d_1 = 10$, and $d_1 = 2.35$, based on surface tension model (III) for inflation proposed in [34], with γ converted to consistent units.

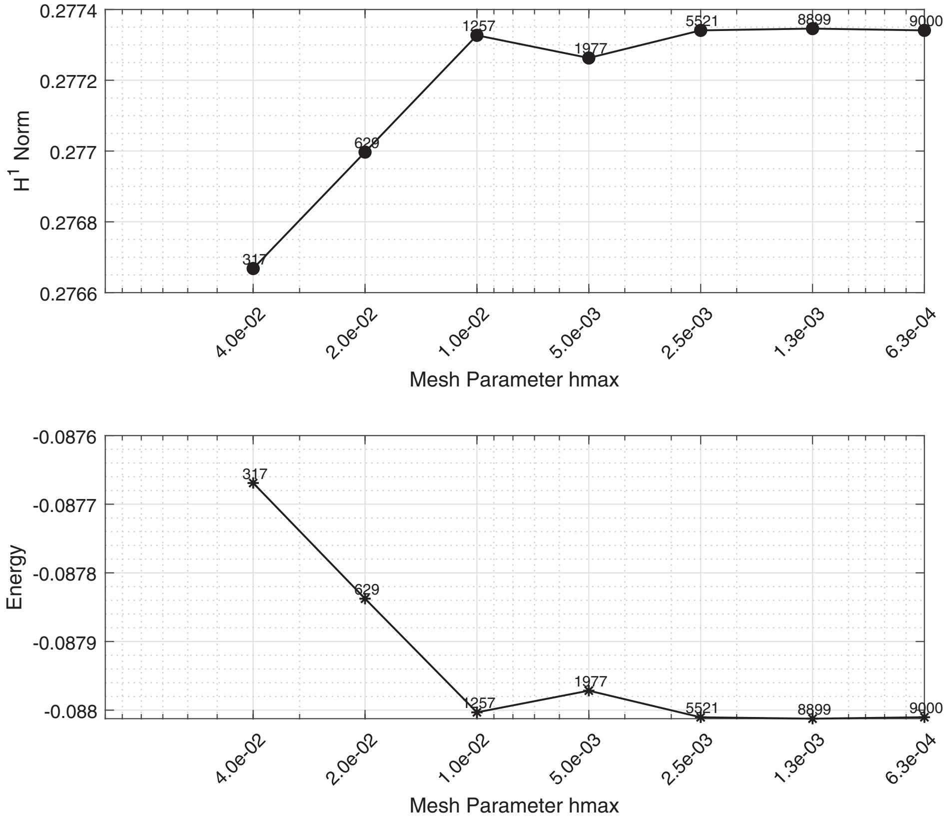

FIGURE 2 | Results of mesh convergence analysis. (Top) H^1 norm of the displacement field against the maximum element size, *hmax*. (Bottom) Total potential energy against *hmax*. In the two plots, the number of elements for each value of *hmax* is shown above the corresponding marker.

values and the maximum simulated pressure of $P = 40$ cmH_2O was imposed. The collagen volume fraction χ was set to its minimum value of 0.05. This was done to evaluate convergence under conditions approaching the material instability limit associated with a pure Neo-Hookean response (i.e., zero collagen). The convergence study involved systematically refining the mesh controlled by the maximum edge size *hmax* used in the *adaptmesh* function, starting from the initial 100×10 rectangular grid while holding all physical inputs constant. In particular, the maximum edge size *hmax* was systematically reduced from 0.04 down to 0.000625. The H^1 norm of the displacement field and the total potential energy are shown in Figure 2. The top plot in Figure 2 shows that the H^1 norm generally increases with refinement and achieves convergence for $hmax \leq 0.0025$, stabilizing near 0.27734. The system energy, plotted in the middle plot of Figure 2, generally decreases as the mesh is refined, consistently with the seek for a minimum energy state. While minor non-monotonic behavior is observed around $hmax = 0.005$, the energy values also stabilize for $hmax \leq 0.0025$, reaching a minimum of approximately -0.08801 at the lowest value of *hmax* (0.000625). The bottom plot of Figure 2 shows that increasing the number of elements beyond approximately 5000 (corresponding to $hmax = 0.0025$) yields negligible changes in the H^1 norm. Based on these results, the value $hmax = 0.0025$ was selected for the subsequent UQ/GSA. This choice provides an accurate solution at a significant computational cost saving (near 5000 elements) compared to finer meshes requiring almost twice as many elements (near 9000) with marginal changes in the chosen metrics.

4 | FEA Numerical Results

In this Section, we present the results of a preliminary numerical study, where all physical parameters were held constant using the fixed and mean values listed in Table 1. As before, the collagen volume fraction χ was fixed at a value of 0.05.

The left-hand side of Figure 3 shows the cross-sectional shapes in the $(2,3)-$ plane (cf. Figure 1c) of the alveolar deformed configurations at equilibrium for a fibrotic tissue stiffness value of $k = 764.78$ cmH_2O at inflation pressure $P = 24$ cmH_2O for increasing values of the fibrotic tissue distribution angle (α). The initial undeformed configuration is represented by a gray dotted line. Lighter color shades corresponding to the smallest distribution angle ($\alpha = -\pi/2$) representing free inflation, i.e., the absence of springs. Progressively darker colors indicate larger distribution angles, with red corresponding to full confinement ($\alpha = \pi/2$), where springs are distributed all around the external alveolar surface. In view of Equation (8), the values $\alpha = -\pi/2, -\pi/4, 0, +\pi/4, +\pi/2$ correspond to surrounding fibrotic tissue area fractions (ϖ) of 0%, 14.6%, 50%, 85.4% and 100%, respectively. All depicted curves account for thickness variation based on the local value of the radial strain λ_r, and show reduced thickness in more inflated regions. As discussed in the previous Section, the deformed configurations for $\alpha = \pm\pi/2$ are calculated as centered at the origin, cf. Equation (18). In Figure 3, for visual comparison, these configurations are translated upwards after imposing the condition $\zeta(-\pi/2) = -1$, while other configurations are unshifted. Inspection of Figure 3 reveals that at small

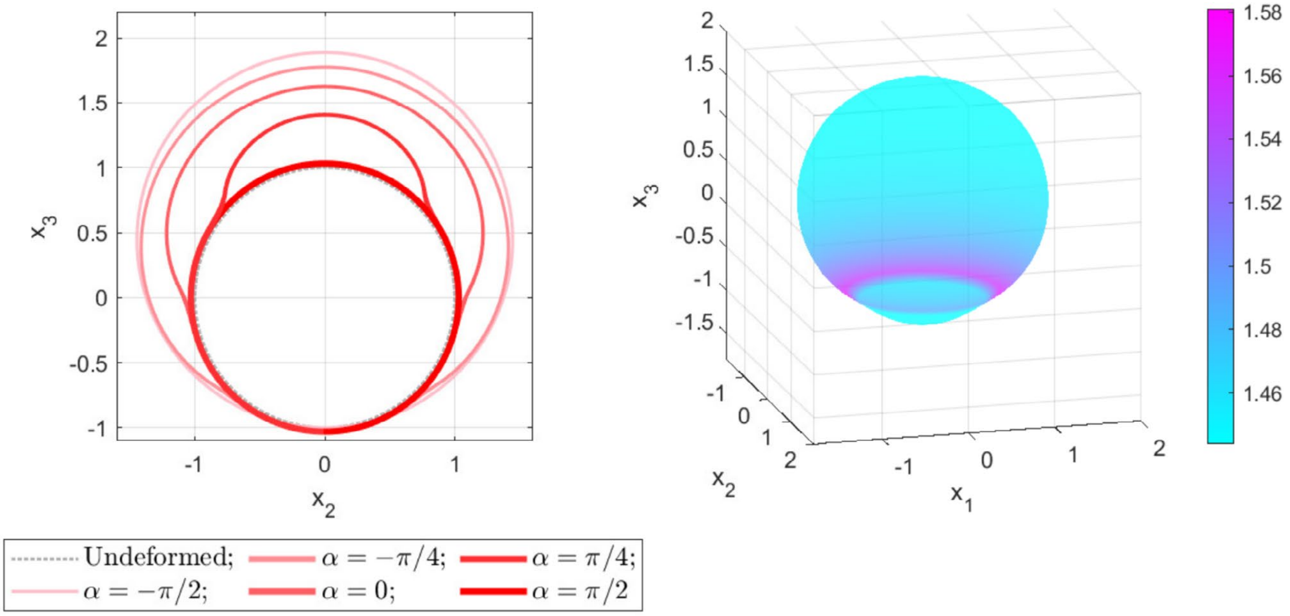

FIGURE 3 | Left: Deformed configurations of an alveolus pressurized at $P = 24\,\mathrm{cmH_2O}$ for increasing values fibrotic tissue distribution angle (α) at a fixed stiffness of fibrotic tissue ($k = 764.78\,\mathrm{cmH_2O}$). Right: Meridian strain (λ_θ) density plot depicted on the deformed configuration of the same alveolus for $\alpha = -\pi/4$. Cyan and pink indicate strains values not greater than and greater than the (uniform) strain of the unconfined alveolus at the same normalized pressure level, respectively.

elevation angles, the deformed and undeformed configurations nearly overlap for all normalized pressures due to confinement by the surrounding fibrotic tissue. As the elevation angle θ increases and approaches α, the deformed configurations deviate, allowing the upper alveolar region to inflate under the action of the internal pressure. Inflation is more pronounced for smaller α values, visually demonstrating the "squishy ball" bulging.

The right-hand side of Figure 3 is a density plot of the meridial strain λ_θ on the alveolar deformed configurations for ($\alpha = -\pi/4$). Cyan indicates strain values not exceeding the uniform strain experienced by the alveolar material during free inflation at the same normalized pressure level, while pink highlights points where strain exceeds the free inflation value. The color bar displays the meridian strain levels. Notably, the regional zone (highlighted in pink) near the transition between the confined to the unconfined regions of the alveolar membrane is subjected to higher meridian strain. This zones is hypothesized to be a potential site of overdistension and epithelial cell damage, even when the macroscopic strain remains within safe limits. In the literature, overdistension is linked to inflammation through mechanosignaling, potentially triggering ventilator-induced lung injury (VILI) [46].

The top, middle and bottom plots in Figure 4 show the strain components λ_θ, λ_ϕ, and λ_r, respectively, as a function of θ for the same values of normalized pressure and fibrotic tissue distribution angles as in the left-hand side Figure 3. The same color scheme is adopted as in Figure 3. In the three plots, the horizontal lines correspond to the cases of non-confinement ($\alpha = -\pi/2$) and full confinement ($\alpha = \pi/2$), where the strain is uniformly distributed, see Equation (18). As expected, the case of non-confinement always presents larger stretches than the case of full confinement. While free inflation and full confinement result in a uniform distension of the alveolar membrane, Figure 4 shows that the curves for the three intermediate confinement cases $\alpha = -\pi/4, 0, +\pi/4$ start at $\theta = -\pi/2$ near the line for $\alpha = -\pi/2$, reach a peak at $\theta = \alpha$ and then decrease, flattening as they approach $\theta = +\pi/2$. In the top plot, strain peaks observed at $\theta = \alpha$ are caused by the transition between confined and unconfined zones, with peak heights decreasing as α increases. For the considered value of P, $\widetilde{k}$ and α, the meridian strain peaks for the two fibrotic tissue distribution angles $\alpha = -\pi/4$ and 0 exceed the free inflation stretch at the same pressure. These numerical results suggest that alveoli surrounded by fibrotic tissue may experience higher meridian strain peaks compared to alveoli in healthy lungs. The middle plot in Figure 4 shows that the circumferential strain, λ_ϕ, increases with elevation, deviating from the fully confined case near $\theta = \alpha$ and approaching the free inflation value at $\theta = \pi/2$. The transition is smooth, with no peaks. The bottom plot in Figure 4 indicates that λ_r decreases with elevation, transitioning from the fully confined value near $\theta = -\pi/2$ to the free inflation value at $\theta = \pi/2$, resulting in thinning near the most inflated region. All curves exhibit a corner at $\theta = \alpha$, which is caused by the transition from confined to unconfined zones.

Figure 5 illustrates the distributions of the meridian (top) and circumferential (middle) stresses, σ_θ and σ_ϕ as a function of θ. The meridian stress distribution has a trend similar to the corresponding strain distribution, with peaks occurring at $\theta = \alpha$, but the stress peak exceeds the free inflation stress only for $\alpha = -\pi/4$ ($\varpi = 14.6\%$). The circumferential stress follows the trend of the circumferential strain, with stress values always below those of free inflation. All curves exhibit a corner at $\theta = \alpha$, due to the transition from confined to unconfined zones. The lower part of the Figure 5 shows the distribution of the contact stress f_k. The contact stress increases with elevation, reaches

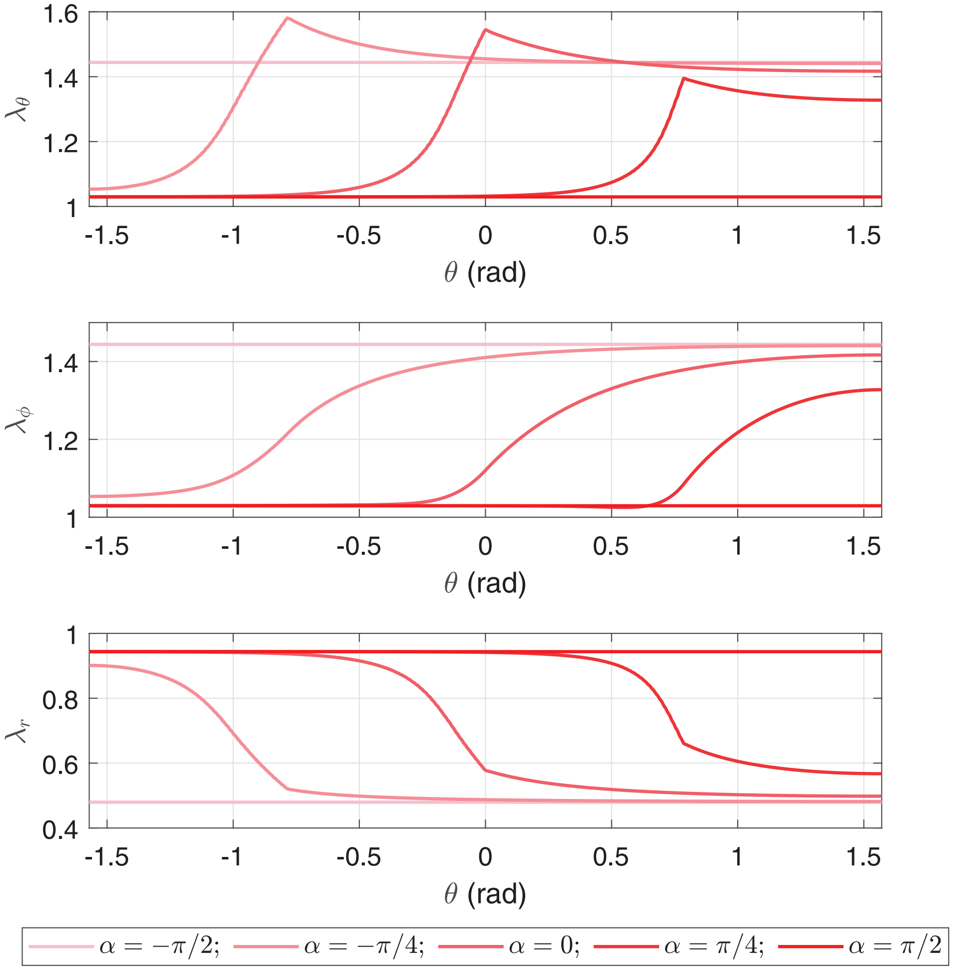

FIGURE 4 | Strain distributions in the meridian direction (top), circumferential direction (middle) and radial direction (bottom) of an alveolus pressurized at $P = 24\,\mathrm{cmH_2O}$ for increasing values fibrotic tissue distribution angle (α) at a fixed stiffness of fibrotic tissue ($k = 764.78\,\mathrm{cmH_2O}$).

a peak at $\theta = \alpha$, and then falls to zero in the unconfined zone. The distribution angle α clearly identifies the spatial location of a highly localized peak in the contact stress. Such peaks may be hypothesized to be key drivers of cellular behavior and could explain spatially heterogeneous responses observed in lung tissue remodeling or disease.

5 | UQ/GSA Analysis

Our computation model, while providing useful insights into strain and stress peaks arising from the confinement provided by the fibrotic tissue, relies on input geometrical and constitutive parameters that are inherently variable in a biological context. To assess the influence of this variability on the model predictions and to identify the most critical parameters, we performed Uncertainty Quantification (UQ) and Global Sensitivity Analysis (GSA).

While UQ is performed to assess the impact of the input uncertainties on the model's predictions, thereby evaluating the robustness of the findings, GSA through the calculation of Sobol indices was employed to identify which uncertain input parameters contribute most significantly to the variability in the outputs, thus highlighting the most influential factors.

In this work, the arbitrary polynomial chaos (aPC) method is adopted to perform UQ and QSA [47]. The first step of the method is the identification of the output quantities of interest (QoIs). To quantify the impact of heterogeneous confinement on the alveolar mechanical environment, five specific QoIs were selected based on their direct relevance to potential mechanotransduction triggers and cell injury. Given the axisymmetric nature of the modeled partial confinement and the resulting bulging deformation, both meridian stress and strain components are critical for characterizing the mechanical state, as highlighted by the numerical results shown in the previous Section. To specifically isolate and quantify the strain and stress peaks due to partial confinement, two primary QoIs were defined as ratios: the ratio of the peak meridian strain under partial confinement to the uniform meridian strain during free inflation at the equivalent pressure level, $\lambda_\theta(\alpha)\,/\,\lambda_s$, and the analogous ratio for the peak meridian stress, $\sigma_\theta(\alpha)\,/\,\sigma_s$. These ratios directly reflect the stress and strain peaks imputable to the “squishy ball” effect. Three more QoIs were defined for our analysis: the peak meridian strain under partial confinement, $\lambda_\theta(\alpha)$, the peak meridian stress under partial confinement, $\sigma_\theta(\alpha)$, and the peak magnitude contact pressure under confinement, $f_k(\alpha)$. The peak meridian strain and stress were chosen because they quantify the maximum local stretch and tensile stress experienced by the alveolar

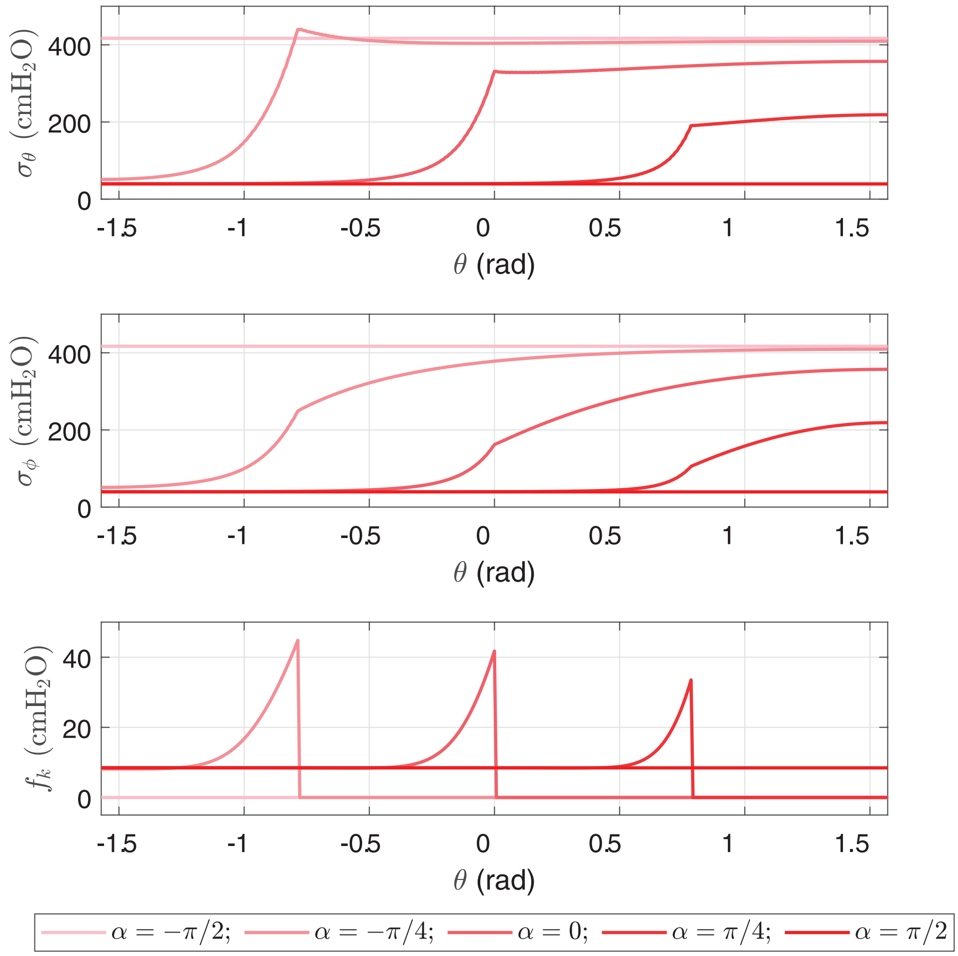

FIGURE 5 | Stress distributions in the meridian direction (top) and in circumferential direction (middle), and magnitude of the contact stress (bottom) of an alveolus pressurized at $P = 24$ cmH$_2$O for increasing values fibrotic tissue distribution angle (α) at a fixed stiffness of fibrotic tissue ($k = 764.78$ cmH$_2$O).

wall. However, these peak values alone do not inherently describe the change induced by the fibrotic heterogeneity compared to the uniform "healthy" baseline. Conversely, the peak meridian stress ratio and the peak meridian strain ratio quantify this relative impact. A high ratio clearly indicates a significant strain or stress amplification due to the "squishy ball" effect, even if the peak strain or stress at that specific pressure or stiffness might be below a critical damage threshold. The peak magnitude contact pressure exerted by the confining fibrotic tissue (the springs) onto the alveolar membrane was selected as another critical QoI, because it represents the resultant of localized compressive and shear forces transmitted directly from the stiff fibrotic region to the adjacent compliant tissue, thereby providing insight into the overall mechanical interaction forces at the boundary of the fibrosis.

Next, eight input (geometrical and constitutive) parameters were defined along with their probability distributions and ranges, as detailed in Table 1. The intrinsic mechanical properties of the alveolar wall were represented by three uncertain parameters: the elastin elasticity parameter (c_1), the collagen elasticity parameter (c_2), and the collagen volume fraction (χ). These parameters are crucial as they define the baseline deformability of the tissue and its tendency to stiffen with increased collagen content, a hallmark of IPF. Both c_1 and c_2 were modeled using lognormal distributions, reflecting their non-negative nature and the typical not symmetrically distributed variability of biological material properties; their statistical parameters were derived from mean values and 95% confidence intervals reported in previous work for healthy lungs [33]. The collagen volume fraction, χ, was modeled using a uniform distribution. The range [0.05,0.29] was selected based on physical considerations of healthy tissue. In particular, the upper bound derived from previous estimates [33], and the lower bound was selected in reference to the mean of 0.102 ± 0.011 reported by Mercer and Crapo [48] for healthy lung parenchyma. While the minimum of 0.05 is lower than their mean, it accounts for potential physiological variability and establishes a baseline for healthy tissue in our simulations. The lower bound of 0.05 also serves to mitigate potential numerical instabilities in the mechanical model associated with vanishing collagen fractions, which correspond to a pure Neo-Hookean material behavior characterized by limit point instability under inflation. The heterogeneity of the fibrotic tissue surrounding the alveolus was represented by two uncertain parameters: the angle of fibrotic tissue distribution α, determining the geometric extent of alveolar confinement, and the stiffness k of the confining fibrotic tissue modeled as a spring distribution. Both α and k were assigned uniform distributions. For α, its full possible range $\left[-\pi/2, \pi/2\right]$ was chosen to explore the entire span of partial confinement. The range for k was derived from literature estimates of tissue stiffness in highly fibrotic regions [44, 45]. Surfactant function can be impaired in IPF [49, 50], and the precise values of these model parameters in vivo carry uncertainty. Accordingly, the surfactant model parameters γ, d_1, and d_2 were all assigned uniform distributions, reflecting a possible $\pm 20\%$ variation around their nominal values based on the surface tension model (III) for inflation proposed in [34]. The whole set of uncertain parameters, comprising material properties, geometric features of fibrosis, and surface tension characteristics, was chosen to provide a robust assessment of the multifactorial influences on alveolar mechanics in the context of IPF.

The aPC MATLAB toolbox *Data-driven Arbitrary Polynomial Chaos* [36, 37, 51] was employed to sample from the input distributions, generate basis polynomials for specified orders of truncation, solve the regression problem and finally evaluate the variability and sensitivity indices. For each sample, numerical simulations were performed using the FEA model implemented in FreeFEM to compute the corresponding outputs. The analysis was conducted for the following six different pressure values: $P = 4.0, 8.0, 16.0, 24.0, 32.0, 40.0\ \mathrm{cmH_2O}$.

Given the pressure scenario, the spectral coefficients of the aPC expansion have to be determined for a maximum polynomial degree p. For the 8 uncertain input parameters considered, this results in a polynomial basis comprising $N_c = \binom{p+8}{p}$ terms, thus requiring the estimation of N_c corresponding coefficients. In this study, with 8 uncertain input parameters, the number of terms for polynomial degrees $p = 3, 4$, and 5 was 165,495, and 1287, respectively. The aPC MATLAB toolbox employs a point collocation method, utilizing Gaussian quadrature nodes as the collocation points for the experimental design, which therefore consists of these N_c points where the full FEA model has to be evaluated. Since Lasso sparse regression was applied to fit the PCE model to these simulation results, the N_c terms for polynomial degrees represent the maximum number of potential terms from which a sparser set of active coefficients was selected for each degree $p = 3, 4$, and 5. FEA simulation success rates for generating the training data were consistently high, with a very low incidence of non-convergent runs. For example, even for the most demanding $p = 5$ expansions (requiring 1287 nominal runs per pressure), the number of failed runs typically ranged from 0 to 3, with a success rate above 99.7%.

For each of the six chosen pressure values, aPC surrogate models were trained using polynomial degrees ranging from $p = 3$ to 5. Polynomial degree $p = 2$ was excluded from the analysis because it consistently resulted in zero estimated variance for one or more QoIs across the pressure scenarios, precluding meaningful GSA for those outputs. To avoid overfitting, the optimal degree for each pressure was determined by selecting the model that minimized the mean Root Mean Squared Error (RMSE), obtained by averaging the individual RMSE values calculated for each QoI on an independent validation dataset (approximately 560 − 599 successful runs *per* pressure value). The chosen optimal degrees and corresponding validation metrics are summarized in Table 2. The surrogate model performance was evaluated using the mean Coefficient of Determination (R^2), obtained by averaging across all five QoIs calculated on the independent validation set for each pressure value. For all pressures from 4 to 40 $\mathrm{cmH_2O}$, the optimal polynomial degree yielded averaged R^2 consistently exceeding 0.95, indicating excellent predictive accuracy and providing a robust foundation for the subsequent UQ and GSA. The UQ and GSA were then performed separately for each pressure value, using the optimal polynomial degree for that specific pressure scenario, as presented in Table 2.

UQ results are presented in Figure 6 and demonstrate a clear pressure-dependent evolution for all considered QoIs. The mean values for all QoIs generally increased with inflation pressure, with peak meridian strain, peak meridian stress, and peak contact pressure showing particularly steep rises. The peak meridian strain ratio also showed an initial increase in its mean before plateauing at higher pressures. Notably, the mean peak meridian strain ratio consistently exceeded unity across all pressure range, indicating a persistent amplification

TABLE 2 | Summary of averaged validation Root Mean Squared Error (RMSE) and averaged coefficient of determination (R^2) for different polynomial degrees (p) across pressure scenarios.

Pressure ($\mathrm{cmH_2O}$)	**Averaged RMSE for polynomial degree (p)**			**Optimal p**	**Averaged R^2 for the optimal p**[b]
	$p=3$[a] **($N_c = 165$)**[c]	**$p=4$**[a] **($N_c = 465$)**[c]	**$p=5$**[a] **($N_c = 1287$)**[c]		
4	1.521	**0.7971**	0.8689	4	0.9610
8	2.801	1.99	**1.336**	5	0.9651
16	4.544	**2.215**	3.545	4	0.9618
24	6.824	4.799	**4.489**	5	0.9583
32	12.12	**7.707**	9.573	4	0.9607
40	20.86	9.569	**7.055**	5	0.9721

Note: To avoid overfitting, the optimal p for each pressure was selected to minimize the averaged validation RMSE (in bold).

[a] Values represent the averaged Root Mean Squared Error (RMSE) calculated across all five QoIs using an independent validation dataset of approximately 560–599 successful FEA runs per pressure scenario.

[b] Values represent the averaged Coefficient of Determination (R^2) calculated across all five QoIs using the independent validation dataset per pressure scenario.

[c] Total number of polynomial basis terms.

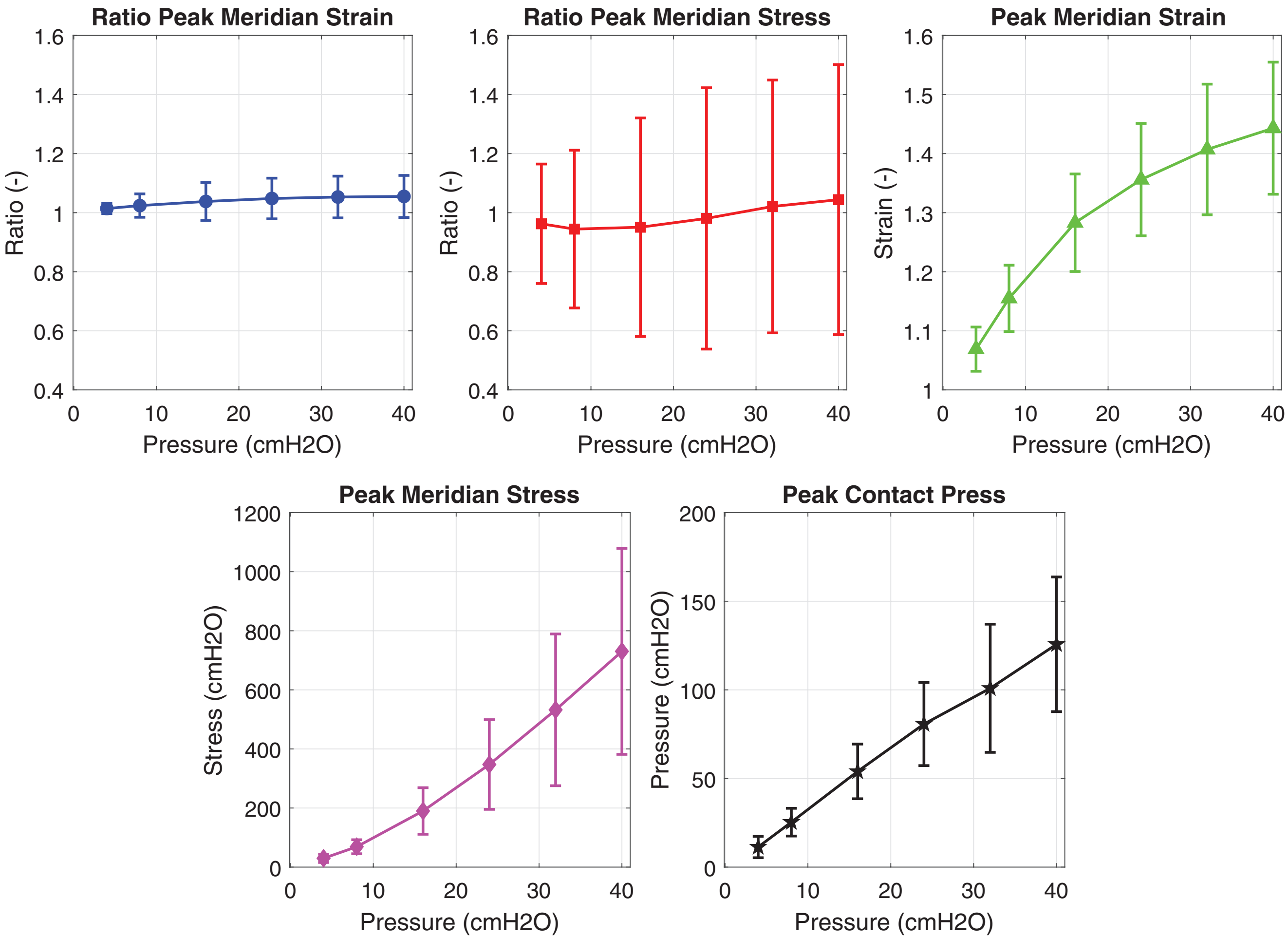

FIGURE 6 | Pressure-dependent evolution of the mean and uncertainty for each quantity of interest (QoI). Markers represent the mean values, and error bars indicate ± 1 standard deviation, as estimated by the validated aPC surrogate models. The plots show an overall increase in the magnitude and variability of the QoIs as inflation pressure increases.

of mechanical load due to heterogeneous confinement, reaching approximately 1.055 at 40 cmH_2O. The mean peak meridian stress ratio exhibited an initial decrease followed by an increase with a widening of the uncertainty band, and reached a value of approximately 1.044 at 40 cmH_2O. The absolute peak strain, stress, and contact pressure exhibited steep increases in their mean values with a widening of their uncertainty bands (standard deviations). This indicates increased variability and magnitude of these potentially injurious stimuli at higher inflation levels. These UQ estimates are derived from surrogate models demonstrating high predictive accuracy (validation $R^2 > 0.95$ across these pressure scenarios), giving strong confidence to these quantitative assessments of output variability.

To clarify the observed variability, a GSA was performed, yielding Total Sobol' Indices (STis) for each input parameter, as represented in Figures 7 and 8. The STi capture the overall importance of a parameter, including its individual contribution and all its interactions with other parameters. The detailed mathematical framework and computational procedures for these indices are well-established and can be found in [47, 52, 53]. The GSA revealed distinct and pressure-dependent parameter trends for different QoIs, highlighting how different parameters govern various aspects of the mechanical response. Given the high fidelity of the underlying surrogate models (validation $R^2 > 0.95$), these sensitivity rankings of variance are considered reliable indicators of parametric influence on the alveolus model's behavior. For the peak meridian strain and stress ratio (Figure 7, top row), the angle of fibrotic tissue distribution, α, is the dominant parameter influencing their variance, with STis values consistently exceeding 0.98 for pressures above 16 cmH_2O. This indicates that the geometric extent of confinement is the primary driver of the relative amplification of strain and stress. In contrast, the STis for the peak meridian strain, the peak meridian stress, and the peak contact pressure display a significant transition in parametric influence with increasing inflation pressure. At low pressures ($P \leq 8$ cmH_2O), the surfactant parameter d_2 associated with the surfactant energy model (cf. Equation (9)) is the most influential factor. However, as pressure increases, the influence of the angle of fibrotic tissue distribution, α, grows, with inverted U-shaped trends for the peak meridian strain and stress, and a more stable trend for the peak contact pressure. Interestingly, the parameter d_2, which dominate the exponential decay of surface tension effects with increasing surface area strain J_2, showed a significantly larger STi for the peak meridian strain, the peak meridian stress, and the peak contact pressure in this low-pressure regime (Figure 7). This is physically intuitive: at smaller area strains characteristic of low inflation, the exponential term is more sensitive to

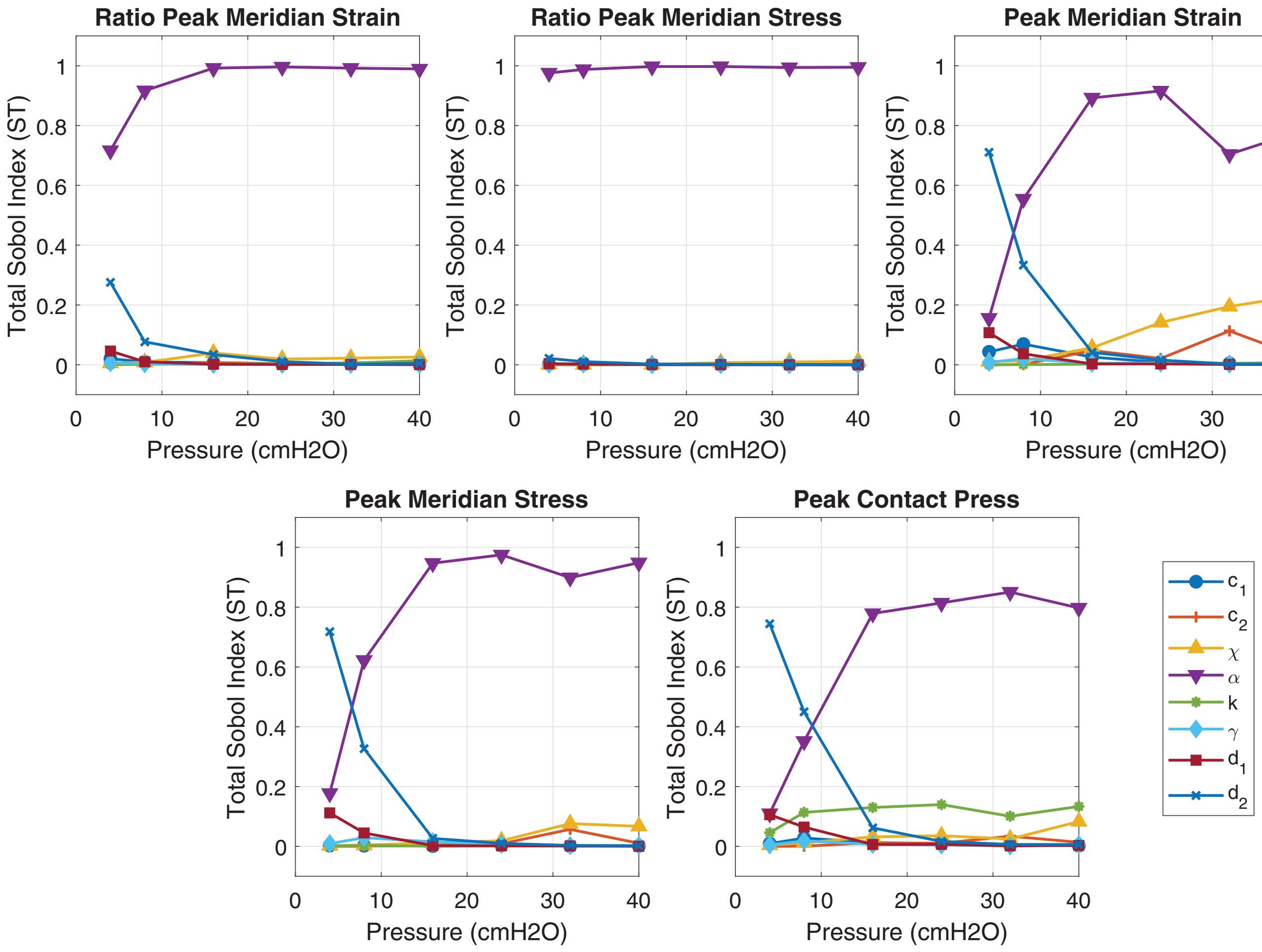

FIGURE 7 | Evolution of total Sobol' indices (STs) with increasing inflation pressure. For the absolute metrics (peak meridian strain, peak meridian stress and peak contact stress), the surfactant parameter d_2 is the most influential parameter at low pressures. However, as pressure increases, the angle of fibrotic tissue distribution, α, dominates all QoIs.

changes in d_2, making the strain-dependent component of surface tension more influential. As pressure and surface strain increase, this exponential term decreases, thereby reducing the impact of d_2. This finding highlights the importance of accurately modeling surfactant properties, particularly their strain-dependent characteristics, for understanding alveolar mechanics at low lung volumes.

The dominance of the angle of fibrotic tissue distribution, α, at larger pressure values for all QoIS and in particular for the two peak ratios, measuring the "squishy ball" effects, indicates the critical role of the geometric constraint induced by the external fibrotic tissue as inflation progresses. The confinement angle α is directly related via Equation (8) to the area fraction of the elastic foundation, ϖ, modeling the extent of fibrotic tissue confining the alveolar deformation. This confirms that the "squishy ball" effect is mostly influenced by the amount of fibrosis and its distribution within the lungs.

6 | Clinical Implications

The results of our study hold significant clinical implications for both patients undergoing spontaneous unassisted breathing and those requiring ventilatory support. Lung protective ventilation is the cornerstone of severe acute respiratory failure management. Clinical and experimental data suggest that excessive strain and airspace epithelial shear stress are critical factors in promoting ventilator-induced lung injury [54]. In the injured lung, such as in acute respiratory distress syndrome (ARDS), the parenchyma becomes mechanically heterogeneous. Many years ago, Mead and colleagues suggest that trans-pulmonary pressure applied to the lung can reach a dangerous threshold at the interface between tissues of different elasticity. Therefore, strain may be greater in areas where the inflated lung is adjacent to the atelectasis areas or fluid-filled alveolar tissue, amplifying lung inflammation, and exacerbating alveolar barrier disruption [55]. Data from randomized clinical trials showed that mechanical ventilation strategies that limit the tidal inflation ($4-8$ mL/kg predicted body weight), and inspiratory pressure applied to respiratory system (plateau pressure $< 30\ \mathrm{cmH_2O}$) significantly improves patient outcome [56]. Thus, it can be hypothesized that protective mechanical ventilation is able to prevent VILI promoting the healing of lung injury at least in a significant proportion of patients suffering from ARDS. The lungs of patients affected by IPF are characterized by a heterogeneous mosaic of contiguous tissue with different elasticity, which result more marked than ARDS. Therefore, the peculiar mechanics of the fibrotic lung could make the concept of protective mechanical ventilation inapplicable in this context.

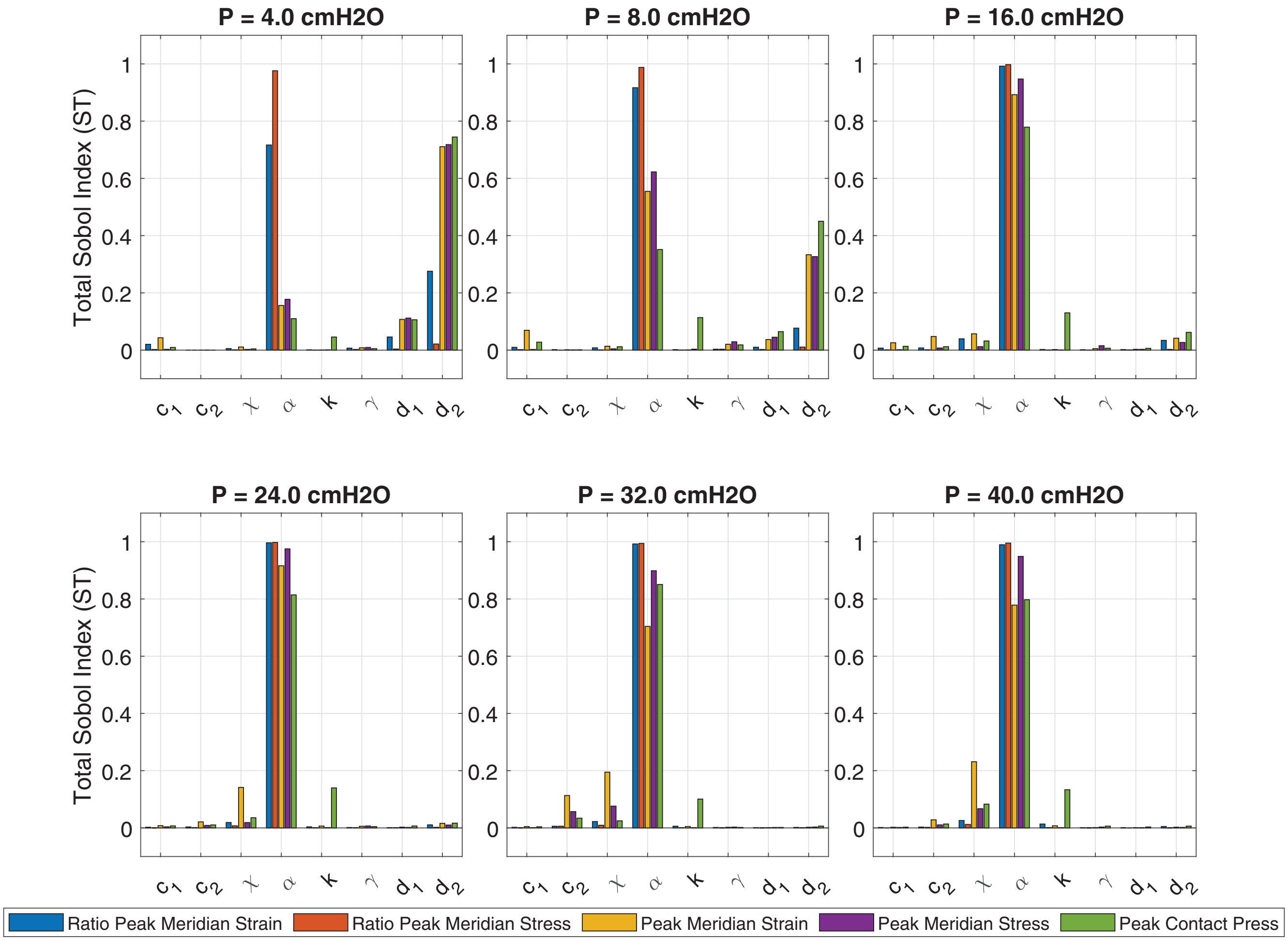

FIGURE 8 | Bar charts of the total Sobol' indices (STs) for all input parameters influencing each QoI. At higher pressure values, the confinement angle, α, becomes the dominant parameter.

The observation that even low-pressure values can cause protrusion of expandable lung tissue due to amplified stress at interfaces with inelastic regions underscores the heightened vulnerability of fibrotic lungs [57]. This increased susceptibility lowers the VILI threshold compared to the pathophysiology observed in ARDS, suggesting that the initiation of mechanical ventilation in fibrotic lungs almost inevitably results in macroscopic damage [58]. Mathematical modeling further validates these findings, highlighting the unique mechanical behavior of fibrotic lungs [33].

On a microscopic level, the "squishy ball" effect—nonphysiological deformation of lung tissue under even minimal applied pressure—may activate profibrotic mechanotransduction pathways [59]. This process likely triggers molecular cascades driving fibrosis progression [9]. The "squishy ball" behavior in the areas of juxtaposition of lung tissues with extremely different mechanical features (fibrosis toward areas of spared lung) could represent the exaggerated mechanical stimulus that triggers the intracellular reaction leading to progressive ECM deposition and tissue destruction. Therefore, this mechanical model of lung fibrosis suggests that fibrosis progression may represent the failure to reestablish mechanical homeostasis. In this line, the unpredictable clinical course of IPF, characterized by rapidly progressive or stable phenotypes [60], could be partially explained by these mechanical triggers, offering a plausible explanation for observed clinical variability [61]. Quantitative imaging analyses have revealed that patients with UIP patterns exhibit hyperinflation even during maximal spontaneous inspiratory efforts [62]. During episodes of respiratory distress, these patients generate intrathoracic pressures that exceed physiological limits [21], a phenomenon that may also occur during physical exertion [63]. This study highlights the potential for fibrosis progression to be driven by even modest respiratory effort, mediated through unbalanced mechanical stress and strain on the lung parenchyma. Our findings emphasize the critical importance of evaluating the mechanical characteristics of fibrotic lungs to identify specific "*mechanotypes*" associated with a higher risk of disease progression. Such evaluations could inform personalized follow-up programs and guide recommendations for lifestyle and physical activity modifications. These tailored interventions aim to mitigate adverse mechanical stress and prevent the activation of profibrotic pathways, ultimately improving clinical outcomes for patients with fibrotic lung disease.

7 | Conclusions

Our study aimed to investigate the mechanical response of an inflated healthy alveolus partially confined by the presence of surrounding fibrotic tissue. The alveolus is modeled as a hyperelastic, homogeneous, non-linear spherical membrane, while the fibrotic tissue is represented as an axisymmetric distribution of linear springs applied on a portion of the external surface. By varying the surface over which the springs are distributed, we simulate various cases. The two limiting cases, the absence of springs and the full coverage of springs, correspond to the free inflation and the full confinement of the alveolar membrane, respectively. In these cases, we find that the deformed configuration of the alveolus takes a spherical shape, which can be calculated in closed form using Equations (18) and (20), along with the corresponding strain and stress components, cf. Equation (16). For partial spring distributions, we compute the deformed configurations numerically using a script implemented in FreeFEM.

To assess the robustness of the predictions of our alveolar model, we performed UQ to determine the range of stress and strain peaks given the parameter uncertainties, as well as GSA to determine the relative importance of each input parameter in driving the model's predictions. UQ and GSA were based on aPC expansions, motivated by their ability to create computationally inexpensive surrogate models that accurately capture the input–output relationship of complex finite element models, thereby enabling efficient uncertainty propagation and sensitivity calculations.

Our study has several limitations. A key assumption in our model is the incompressibility of the alveolar wall material. While frequently employed for soft tissues due to their high water content, lung parenchyma, as a porous fiber network, can exhibit compressible and potentially more complex volumetric behaviors [64, 65]. In the present study, the incompressibility assumption was retained because it ensures consistency with our previous work from which estimates of the material parameters (e.g., the elasticity parameters c_1 and c_2, and the collagen volume fraction χ) were derived. These parameters were obtained by fitting an incompressible hyperelastic model to clinical data of pressure-volume curves [33]. Relaxing this assumption would need a complete re-parameterization of the material model, which is beyond the scope of the current investigation. Future work should aim to address this limitation by developing and incorporating compressible constitutive models for the alveolar wall. This would involve re-deriving material parameters from experimental data that explicitly accounts for compressibility and subsequently re-evaluating the stress/strain environment and parameter sensitivities.

Another limitation of the present study is the assumption of axial symmetry, which is at the basis of the analytical homogenization yielding Equation (7). A future direction would be to generalize the model by employing more advanced multiscale modeling techniques, such as asymptotic homogenization [32, 66]. This technique is powerful in providing macroscale models that encode information about the microstructure of the material, particularly all the elastic subphases embedded in the matrix, such as elastin, collagen fibers, and fibroblasts. Interestingly, asymptotic homogenization techniques can also be applied when the material undergoes large deformations, as in the case of lung parenchyma [31]. This could lead to the development of new, more sophisticated models that could better capture the behavior of the entire system.

Another simplifying assumption was to perform the stress/strain analysis at the scale of a single alveolus, neglecting broader lung anatomy, regional heterogeneity caused by gravity, or intrinsic local tissue variability. Additionally, the model focuses exclusively on elastic effects under static inflation, without accounting for viscoelasticity. The lung parenchyma is a complex composite whose response is inherently time-dependent due to the viscoelastic nature of the solid matrix and fluid–solid interaction of poroelasticity. While our current framework captures the equilibrium state, a future extension that incorporates viscoelastic constitutive laws is essential to model the dynamics of the breathing cycle. This includes phenomena like stress relaxation and pressure-volume hysteresis. This dynamic model would naturally lead to a poroelastic formulation, enabling a more thorough examination of the interaction between tissue mechanics and fluid flow during ventilation in healthy and fibrotic lungs.

A key finding of our study is the emergence of strain peaks in the meridian direction of partially confined alveolar membranes. These strain peaks result from the transition between the confined and the unconfined zones. Unconfined zones are numerically predicted to bulge outward in a “squishy” manner. Notably, FEA results indicate that the strain and stress peaks may exceed the uniform strain calculated during free inflation at the same pressure level. Based on these findings, we hypothesize that regions near the transitions between confined and unconfined areas may serve as potential sites of overdistension and epithelial cell damage, even when the overall macroscopic strain remains within safe limits.

In conclusion, while acknowledging the simplifications inherent in our model, this work provides quantitative evidence for the generation of localized, supra-physiological mechanical stresses at the microscale due to tissue heterogeneity in IPF. Uncertainty quantification demonstrated that these predicted strain and stress peaks are robust features of the heterogeneous system, consistently emerging despite variations in key model parameters. Our findings, further supported by global sensitivity analysis which identified the confinement angle as the primary determinant factor of peak strain/stress magnitudes, underline the importance of the local mechanical environment in disease progression. This provides a quantitative framework for future investigations into the downstream biological responses, such as $\mathrm{TGF}-\beta 1$ activation and fibroblast behavior, at these mechanically active interfaces. Our model identifies regions of potential overdistension and highlights where pro-fibrotic signaling, such as $\mathrm{TGF}-\beta 1$ activation and altered fibroblast behavior, is most likely to occur. To capture disease progression, we plan to integrate these findings with growth and remodeling models in the future. This would require developing a coupled mechanobiological framework in which predicted stress concentrations are coupled with a cell behavior model. This model would then update local tissue properties, thereby simulating the vicious cycle of stiffening and disease progression that is the hallmark of fibrosis.

To experimentally validate our findings, future studies could take advantage of in vitro models mimicking alveolar heterogeneity, such as micropatterned substrates with tunable stiffness, or ex vivo tissue systems, where advanced imaging techniques can map local strain and stress distributions under load and correlate these with cellular mechanosensitive responses at predicted stress and strain concentration sites.

Author Contributions

Raffaella Rizzoni, **Roberto Tonelli**, **Alessandro Marchioni:** conceptualization. **Raffaella Rizzoni:** formal analysis. **Raffaella Rizzoni**, **Roberto Tonelli**, **Alessandro Marchioni:** investigation. **Raffaella Rizzoni:** methodology. **Raffaella Rizzoni**, **Roberto Tonelli**, **Alessandro Marchioni:** project administration. **Raffaella Rizzoni:** resources and software. **Raffaella Rizzoni**, **Roberto Tonelli**, **Alessandro Marchioni:** supervision and validation. **Raffaella Rizzoni:** visualization. **Raffaella Rizzoni**, **Roberto Tonelli**, **Alessandro Marchioni:** writing – original draft preparation. **Raffaella Rizzoni**, **Roberto Tonelli**, **Alessandro Marchioni:** writing – review and editing.

Acknowledgments

This research has been conducted according to the inspiring scientific principles of the Italian National Group for the Mathematical Physics (GNFM) of the National Institute for Advanced Mathematics (INdAM).

Funding

The authors have nothing to report.

Ethics Statement

The authors have nothing to report.

Conflicts of Interest

The authors declare no conflicts of interest.

Data Availability Statement

Data sharing not applicable to this article as no datasets were generated or analysed during the current study.

References

1. F. Martino, A. Perestrelo, V. Vinarský, S. Pagliari, and G. Forte, “Cellular Mechanotransduction: From Tension to Function,” *Frontiers in Physiology* 9 (2018): 824, https://doi.org/10.3389/fphys.2018.00824.

2. X. Di, X. Gao, L. Peng, et al., “Cellular Mechanotransduction in Health and Diseases: From Molecular Mechanism to Therapeutic Targets,” *Signal Transduction and Targeted Therapy* 8, no. 1 (2023): 282, https://doi.org/10.1038/s41392-023-01501-9.

3. J. Humphrey, E. Dufresne, and M. Schwartz, “Mechanotransduction and Extracellular Matrix Homeostasis,” *Nature Reviews. Molecular Cell Biology* 15, no. 12 (2014): 802–812, https://doi.org/10.1038/nrm3896.

4. D. Tschumperlin, “Matrix, Mesenchyme, and Mechanotransduction,” *Annals of the American Thoracic Society* 12, no. 1 (2015): S24–S29, https://doi.org/10.1513/AnnalsATS.201407-320MG.

5. C. Lin, X. Zheng, Y. Lin, J. Wu, and Y. Li, “Mechanotransduction Regulates the Interplays Between Alveolar Epithelial and Vascular Endothelial Cells in Lung,” *Frontiers in Physiology* 13 (2022): 818394, https://doi.org/10.3389/fphys.2022.818394.

6. Z. Deng, M. Fear, Y. Suk Choi, et al., “The Extracellular Matrix and Mechanotransduction in Pulmonary Fibrosis,” *International Journal of Biochemistry & Cell Biology* 126 (2020): 105802, https://doi.org/10.1016/j.biocel.2020.105802.

7. G. Raghu, M. Remy-Jardin, L. Richeldi, et al., “Idiopathic Pulmonary Fibrosis (An Update) and Progressive Pulmonary Fibrosis in Adults: An Official ATS/ERS/JRS/ALAT Clinical Practice Guideline,” *American Journal of Respiratory and Critical Care Medicine* 205, no. 9 (2022): e18–e47, https://doi.org/10.1164/rccm.202202-0399ST.

8. P. Wolters, H. Collard, and K. Jones, “Pathogenesis of Idiopathic Pulmonary Fibrosis,” *Annual Review of Pathology* 9 (2014): 157–179, https://doi.org/10.1146/annurev-pathol-012513-104706.

9. A. Marchioni, R. Tonelli, S. Cerri, et al., “Pulmonary Stretch and Lung Mechanotransduction: Implications for Progression in the Fibrotic Lung,” *International Journal of Molecular Sciences* 22, no. 12 (2021): 6443, https://doi.org/10.3390/ijms22126443.

10. W. D. Hardie, S. W. Glasser, and J. S. Hagood, “Emerging Concepts in the Pathogenesis of Lung Fibrosis,” *American Journal of Pathology* 175, no. 1 (2009): 3–16, https://doi.org/10.2353/ajpath.2009.081170.

11. A. Samarelli, R. Tonelli, A. Marchioni, et al., “Fibrotic Idiopathic Interstitial Lung Disease: The Molecular and Cellular Key Players,” *International Journal of Molecular Sciences* 22, no. 16 (2021): 8952, https://doi.org/10.3390/ijms22168952.

12. M. Moore and E. Herzog, “Regulation and Relevance of Myofibroblast Responses in Idiopathic Pulmonary Fibrosis,” *Current Pathobiology Reports* 1 (2013): 199–208, https://doi.org/10.1007/s40139-013-0017-8.

13. R. Wells, “Tissue Mechanics and Fibrosis,” *Biochimica et Biophysica Acta* 1831, no. 7 (2013): 884–890, https://doi.org/10.1016/j.bbadis.2013.02.007.

14. F. Liu, J. D. Mih, B. S. Shea, et al., “Feedback Amplification of Fibrosis Through Matrix Stiffening and COX-2 Suppression,” *Journal of Cell Biology* 190, no. 4 (2010): 693–706, https://doi.org/10.1083/jcb.201004082.

15. A. Froese, C. Shimbori, P. Bellaye, et al., “Stretch-Induced Activation of Transforming Growth Factor-$\beta 1$ In Pulmonary Fibrosis,” *American Journal of Respiratory and Critical Care Medicine* 194, no. 1 (2016): 84–96, https://doi.org/10.1164/rccm.201508-1638OC.

16. D. Tschumperlin, G. Ligresti, M. Hilscher, and V. Shah, “Mechanosensing and Fibrosis,” *Journal of Clinical Investigation* 128, no. 1 (2018): 74–84, https://doi.org/10.1172/JCI93561.

17. N. Murata, S. Ito, K. Furuya, et al., “Ca2+ Influx and ATP Release Mediated by Mechanical Stretch in Human Lung Fibroblasts,” *Biochemical and Biophysical Research Communications* 453, no. 1 (2014): 101–105, https://doi.org/10.1016/j.bbrc.2014.09.063.

18. S. Rahaman, L. Grove, S. Paruchuri, et al., “TRPV4 Mediates Myofibroblast Differentiation and Pulmonary Fibrosis in Mice,” *Journal of Clinical Investigation* 124, no. 12 (2014): 5225–5238, https://doi.org/10.1172/JCI75331.

19. B. Hinz and B. Suki, “Does Breathing Amplify Fibrosis?,” *American Journal of Respiratory and Critical Care Medicine* 194, no. 1 (2016): 9–11, https://doi.org/10.1164/rccm.201601-0149ED.

20. C. Upagupta, C. Shimbori, R. Alsilmi, and M. Kolb, “Matrix Abnormalities in Pulmonary Fibrosis,” *European Respiratory Review* 27, no. 148 (2018): 180033, https://doi.org/10.1183/16000617.0033-2018.

21. R. Tonelli, I. Castaniere, A. Cortegiani, et al., “Inspiratory Effort and Respiratory Mechanics in Patients With Acute Exacerbation of Idiopathic Pulmonary Fibrosis: A Preliminary Matched Control Study,” *Pulmonology* 29, no. 6 (2023): 469–477, https://doi.org/10.1016/j.pulmoe.2022.08.004.

22. A. Marchioni, R. Tonelli, G. Rossi, et al., “Ventilatory Support and Mechanical Properties of the Fibrotic Lung Acting as a ‘Squishy Ball’,” *Annals of Intensive Care* 10, no. 1 (2020): 13, https://doi.org/10.1186/s13613-020-0632-6.

23. J. Holland, J. Milic-Emili, P. Macklem, and D. Bates, “Regional Distribution of Pulmonary Ventilation and Perfusion in Elderly Subjects,” *Journal of Clinical Investigation* 47, no. 1 (1968): 81–92, https://doi.org/10.1172/JCI105717.

24. J. Leonard-Duke, S. Evans, R. T. Hannan, et al., “Multi-Scale Models of Lung Fibrosis,” *Matrix Biology* 91-92 (2020): 35–50, https://doi.org/10.1016/j.matbio.2020.04.003.

25. J. K. Hall, J. H. Bates, R. Krishnan, et al., "Elucidating the Interaction Between Stretch and Stiffness Using an Agent-Based Spring Network Model of Progressive Pulmonary Fibrosis," *Frontiers in Network Physiology* 4 (2024): 9–11, https://doi.org/10.3389/fnetp.2024.1396383.

26. D. E. Hurtado, N. Villarroel, J. Retamal, G. Bugedo, and A. Bruhn, "Improving the Accuracy of Registration-Based Biomechanical Analysis: A Finite Element Approach to Lung Regional Strain Quantification," *IEEE Transactions on Medical Imaging* 35, no. 2 (2016): 580–588, https://doi.org/10.1109/TMI.2015.2483744.

27. D. E. Hurtado, B. Erranz, F. Lillo, et al., "Progression of Regional Lung Strain and Heterogeneity in Lung Injury: Assessing the Evolution Under Spontaneous Breathing and Mechanical Ventilation," *Annals of Intensive Care* 10 (2020): 107–117, https://doi.org/10.1186/s13613-020-00725-0.

28. F. Concha, M. Sarabia-Vallejos, and D. Hurtado, "Micromechanical Model of Lung Parenchyma Hyperelasticity," *Journal of the Mechanics and Physics of Solids* 112 (2018): 126–144, https://doi.org/10.1016/j.jmps.2017.11.021.

29. C. Patte, P. Y. Brillet, C. Fetita, et al., "Estimation of Regional Pulmonary Compliance in Idiopathic Pulmonary Fibrosis Based on Personalized Lung Poromechanical Modeling," *Journal of Biomechanical Engineering* 144, no. 9 (2022): 091008, https://doi.org/10.1115/1.4054106.

30. C. Laville, C. Fetita, T. Gille, et al., "Comparison of Optimization Parametrizations for Regional Lung Compliance Estimation Using Personalized Pulmonary Poromechanical Modeling," *Biomechanics and Modeling in Mechanobiology* 22 (2023): 1541–1554, https://doi.org/10.1007/s10237-023-01691-9.

31. L. Miller and R. Penta, "Homogenized Balance Equations for Nonlinear Poroelastic Composites," *Applied Sciences* 11 (2021): 6611, https://doi.org/10.3390/app11146611.

32. L. Miller and R. Penta, "Effective Double-Poroelasticity Derived via Homogenization of Two Non-Interacting Solid Phases Percolated by a Viscous Fluid," *European Journal of Mechanics - A/Solids* 105 (2024): 105219, https://doi.org/10.1016/j.euromechsol.2023.105219.

33. R. Tonelli, R. Rizzoni, S. Grasso, et al., "Stress–Strain Curve and Elastic Behavior of the Fibrotic Lung With Usual Interstitial Pneumonia Pattern During Protective Mechanical Ventilation," *Scientific Reports* 14 (2024): 13158, https://doi.org/10.1038/s41598-024-63670-z.

34. R. Kowe, R. Schroter, F. Matthews, and D. Hitchings, "Analysis of Elastic and Surface Tension Effects in the Lung Alveolus Using Finite Element Methods," *Journal of Biomechanics* 19 (1986): 541–549, https://doi.org/10.1016/0021-9290(86)90127-2.

35. F. Hecht, "New development in FreeFem++," *Journal of Numerical Mathematics* 20, no. 3–4 (2012): 251–266, https://doi.org/10.1515/jnum-2012-0013.

36. S. Oladyshkin, "aPC Matlab Toolbox: Data-Driven Arbitrary Polynomial Chaos, MATLAB Central File Exchange," 2025.

37. S. Oladyshkin and W. Nowak, "Data-Driven Uncertainty Quantification Using the Arbitrary Polynomial Chaos Expansion," *Reliability Engineering and System Safety* 106 (2012): 179–190, https://doi.org/10.1016/j.ress.2012.05.002.

38. C. Wex, S. Arndt, A. Stoll, C. Bruns, and Y. Kupriyanova, "Isotropic Incompressible Hyperelastic Models for Modelling the Mechanical Behaviour of Biological Tissues: A Review," *Biomedical Engineering* 60, no. 6 (2015): 577–592, https://doi.org/10.1515/bmt-2014-0146.

39. R. James and R. Rizzoni, "Pressurized Shape Memory Thin Films," *Journal of Elasticity* 59 (2000): 399–436, https://doi.org/10.1023/A:1011011623270.

40. K. J. Bathe, *Finite Element Procedures* (Prentice Hall, 2006).

41. K. Atkinson, *Numerical Analysis* (John Wiley & Sons, 1989).

42. *MATLAB. Version: 24.1 (R2024a)* (MathWorks Inc., 2024).

43. S. B. Jawde, K. Karrobi, D. Roblyer, et al., "Inflation Instability in the Lung: An Analytical Model of a Thick-Walled Alveolus With Wavy Fibres Under Large Deformations," *Journal of the Royal Society Interface* 18 (2021): 20210594, https://doi.org/10.1098/rsif.2021.0594.

44. A. Booth, R. Hadley, A. Cornett, et al., "Acellular Normal and Fibrotic Human Lung Matrices as a Culture System for in Vitro Investigation," *American Journal of Respiratory and Critical Care Medicine* 186 (2012): 866–876, https://doi.org/10.1164/rccm.201204-0754OC.

45. F. Liu, D. Lagares, K. Choi, et al., "Mechanosignaling Through YAP and TAZ Drives Fibroblast Activation and Fibrosis," *American Journal of Physiology. Lung Cellular and Molecular Physiology* 308, no. 4 (2015): L344–L357, https://doi.org/10.1152/ajplung.00300.2014.

46. L. Gattinoni, E. Carlesso, P. Cadringher, F. Valenza, F. Vagginelli, and D. Chiumello, "Physical and Biological Triggers of Ventilator-Induced Lung Injury and Its Prevention," *European Respiratory Journal. Supplement* 47 (2003): 15s–25s, https://doi.org/10.1183/09031936.03.00021303.

47. V. G. Eck, W. P. Donders, J. Sturdy, et al., "A Guide to Uncertainty Quantification and Sensitivity Analysis for Cardiovascular Applications," *International Journal of Numerical Methods in Biomedical Engineering* 32, no. 8 (2016): e02755, https://doi.org/10.1002/cnm.2755.

48. R. R. Mercer and J. D. Crapo, "Spatial Distribution of Collagen and Elastin Fibers in the Lungs," *Journal of Applied Physiology* 69, no. 2 (1990): 756–765, https://doi.org/10.1152/jappl.1990.69.2.756.

49. A. Gunther, R. Schmidt, F. Nix, et al., "Surfactant Abnormalities in Idiopathic Pulmonary Fibrosis, Hypersensitivity Pneumonitis and Sarcoidosis," *European Respiratory Journal* 14, no. 3 (1999): 565–573, https://doi.org/10.1034/j.1399-3003.1999.14c14.x.

50. E. Lopez-Rodriguez, C. Boden, M. Echaide, et al., "Surfactant Dysfunction During Overexpression of TGF-β1 Precedes Profibrotic Lung Remodeling in Vivo," *American Journal of Physiology. Lung Cellular and Molecular Physiology* 310, no. 11 (2016): L1260–L1271, https://doi.org/10.1152/ajplung.00065.2016.

51. S. Oladyshkin, F. de Barros, and W. Nowak, "Global Sensitivity Analysis: A Flexible and Efficient Framework With an Example From Stochastic Hydrogeology," *Advances in Water Resources* 37 (2012): 10–22, https://doi.org/10.1016/j.advwatres.2011.11.001.

52. I. Sobol', "Global Sensitivity Indices for Nonlinear Mathematical Models and Their MonteCarlo Estimates," *Mathematics and Computers in Simulation* 55, no. 1 (2001): 271–280, https://doi.org/10.1016/S0378-4754(00)00270-6.

53. A. Saltelli, A. Ratto, T. Andres, et al., *Global Sensitivity Analysis: The Primer* (John Wiley & Sons, Ltd, 2007).

54. J. Marini, P. Rocco, and L. Gattinoni, "Static and Dynamic Contributors to Ventilator-Induced Lung Injury in Clinical Practice. Pressure, Energy, and Power," *American Journal of Respiratory and Critical Care Medicine* 201, no. 7 (2020): 767–774, https://doi.org/10.1164/rccm.201908-1545CI.

55. J. Mead, T. Takishima, and D. Leith, "Stress Distribution in Lungs: A Model of Pulmonary Elasticity," *Journal of Applied Physiology* 28 (1970): 596–608, https://doi.org/10.1152/jappl.1970.28.5.596.

56. N. Qadir, S. Sahetya, L. Munshi, et al., "An Update on Management of Adult Patients With Acute Respiratory Distress Syndrome: An Official American Thoracic Society Clinical Practice Guideline," *American Journal of Respiratory and Critical Care Medicine* 209, no. 1 (2024): 24–36, https://doi.org/10.1164/rccm.202311-2011ST.

57. J. Mooney, K. Raimundo, E. Chang, and M. Broder, "Mechanical Ventilation in Idiopathic Pulmonary Fibrosis: A Nationwide Analysis of Ventilator Use, Outcomes, and Resource Burden," *BMC Pulmonary Medicine* 17 (2017): 84, https://doi.org/10.1186/s12890-017-0426-2.

58. R. Tonelli, S. Grasso, A. Cortegiani, et al., "Physiological Effects of Lung-Protective Ventilation in Patients With Lung Fibrosis and Usual Interstitial Pneumonia Pattern Versus Primary ARDS: A Matched-Control Study," *Critical Care* 27 (2023): 398, https://doi.org/10.1186/s13054-023-04682-5.

59. R. K. Albert, P. Smith, C. E. Perlman, and D. A. Schwartz, "Is Progression of Pulmonary Fibrosis due to Ventilation-Induced Lung Injury?," *American Journal of Respiratory and Critical Care Medicine* 200, no. 2 (2019): 140–151, https://doi.org/10.1164/rccm.201903-0497PP.

60. A. Wong, C. Ryerson, and S. Guler, "Progression of Fibrosing Interstitial Lung Disease," *Respiratory Research* 21 (2020): 32, https://doi.org/10.1186/s12931-020-1296-3.

61. A. Wells, K. Brown, and V. Cottin, "The Progressive Fibrotic Phenotype in Current Clinical Practice," *Current Opinion in Pulmonary Medicine* 27, no. 5 (2021): 368–373, https://doi.org/10.1097/MCP.0000000000000805.

62. R. Tonelli, M. Smit, I. Castaniere, et al., "Quantitative CT-Analysis of Over Aerated Lung Tissue and Correlation With Fibrosis Extent in Patients With Idiopathic Pulmonary Fibrosis," *Respiratory Research* 25, no. 1 (2024): 359, https://doi.org/10.1186/s12931-024-02970-4.

63. J. Burdon, K. Killian, and N. Jones, "Pattern of Breathing During Exercise in Patients With Interstitial Lung Disease," *Thorax* 38 (1983): 778–784, https://doi.org/10.1136/thx.38.10.778.

64. S. Rausch, C. Martin, P. Bornemann, S. Uhlig, and W. Wall, "Material Model of Lung Parenchyma Based on Living Precision-Cut Lung Slice Testing," *Journal of the Mechanical Behavior of Biomedical Materials* 4, no. 4 (2011): 583–592, https://doi.org/10.1016/j.jmbbm.2011.01.006.

65. A. Birzle, S. Hobrack, C. Martin, S. Uhlig, and W. Wall, "Constituent-Specific Material Behavior of Soft Biological Tissue: Experimental Quantification and Numerical Identification for Lung Parenchyma," *Biomechanics and Modeling in Mechanobiology* 18 (2019): 1383–1400, https://doi.org/10.1007/s10237-019-01151-3.

66. R. Penta and A. Gerisch, "An Introduction to Asymptotic Homogenization," in *Multiscale Models in Mechano and Tumor Biology*, ed. A. Gerisch, R. Penta, and J. Lang (Springer International Publishing, 2017), 1–26.

Appendix A

FreeFEM Implementation

Listing 1: This appendix contains the FreeFEM script used for the FEA of the axisymmetric alveolar model. The script defines the geometry, mesh (with parameters for initial meshing and adaptmesh), material properties (including tissue elasticity and surfactant model), boundary conditions (including spring confinement), and solves for the equilibrium configuration by minimizing the total potential energy (12).

```
// Parameters
real Pa=24.0/(0.05*53.24); //applied pressure
real k1=75*10.1972/(0.05*53.24); //spring stiffness for the confined zone
real k2=0; //vanishing stiffness for the unconfined zone
real De=0.05; //collagen volume fraction
real g=365.0/53.24; //gamma, ratio of c_2 to c_1
real an1=pi/4; //confinement angle
real l=1.02; //initial strain for the Newton's method
real gam=0.00040788*100/(0.05*53.24*0.011526); //maximum surface tension normalized by c_1
real d1=10.0; //first surfactant parameter
real d2=2.35; //second surfactant parameter
real hmaxval=0.0025 ; //optimized value for hmax in the mesh adaptation
real hminval=0.0001 ;  //chosen value for hmin in the mesh adaptation
int nc=400;

// Macro
macro l1(u, v) (sqrt(dx(u)*dx(u) + dx(v)*dx(v))) //meridian strain lambda_1
macro dl1(u, v, uu, vv) ((dx(u)*dx(uu) + dx(v)*dx(vv))/l1(u,v)) //first variation of lambda_1
macro ddl1(u, v, uu, vv, uuu, vvv) ((dx(uu)*dx(uuu) + dx(vv)*dx(vvv))/l1(u,v)
-((dx(u)*dx(uu) + dx(v)*dx(vv))*(dx(u)*dx(uuu) + dx(v)*dx(vvv)))/(l1(u,v))^3) //second variation of
lambda_1

macro l2(u) (u) //circumferential strain lambda_2
macro dl2(uu) (uu)  //first variation of lambda_2
//macro ddl2(uuu) (0)   //second variation of lambda_2

macro f(l1, l2, chi, g) ((1-chi)*(l1^2+l2^2+1/(l1^2*l2^2)-3)
   +chi*g*(l1^2+l2^2+1/(l1^2*l2^2)-3)^3) //strain energy density (w)
macro df1(l1, l2, chi, g) ((1-chi)*(2.0*l1-2.0/(l1^3*l2^2))
   +3.0*chi*g*(l1^2+l2^2+1/(l1^2*l2^2)-3)^2*(2.0*l1-2.0/(l1^3*l2^2))) //w,1
macro df2(l1, l2, chi, g) ((1-chi)*(2.0*l2-2.0/(l1^2*l2^3))
   +3.0*chi*g*(l1^2+l2^2+1/(l1^2*l2^2)-3)^2*(2.0*l2-2.0/(l1^2*l2^3))) //w,2
macro ddf11(l1, l2, chi, g) ((1-chi)*(2.0+6.0/(l1^4*l2^2))
   +6.0*chi*g*(l1^2+l2^2+1/(l1^2*l2^2)-3)*(2.0*l1-2.0/(l1^3*l2^2))^2
          +3.0*chi*g*(l1^2+l2^2+1/(l1^2*l2^2)-3)^2*(2.0+6.0/(l1^4*l2^2))) //w,11
macro ddf22(l1, l2, chi, g) ((1-chi)*(2.0+6.0/(l1^2*l2^4))+
   6.0*chi*g*(l1^2+l2^2+1/(l1^2*l2^2)-3)*(2.0*l2-2.0/(l1^2*l2^3))^2
       +3.0*chi*g*(l1^2+l2^2+1/(l1^2*l2^2)-3)^2*(2.0+6.0/(l1^2*l2^4))) //w,22
macro ddf12(l1, l2, chi, g) ((1-chi)*4.0/(l1^3*l2^3)
   +6.0*chi*g*(2.0*l1-2.0/(l1^3*l2^2))*(2.0*l2-2.0/(l1^2*l2^3))*(l1^2+l2^2+1/(l1^2*l2^2)-3)
          +12.0*chi*g*(l1^2+l2^2+1/(l1^2*l2^2)-3)^2*1/(l1^3*l2^3)) //w,12

macro V(u, v) (0.5*u^2*dx(v)) //volume integrand
macro dV(u, v, uu, vv) (u*uu*dx(v)+0.5*u^2*dx(vv)) //volume first variation
macro ddV(u, v, uu, vv, uuu, vvv) (uuu*uu*dx(v)+u*uu*dx(vvv)+u*uuu*dx(vv)) //volume second variation

//Surfactant
macro G(A,fam,c1,c2) (fam*(A+(c1/c2)*exp(-c2*A))) //surface energy density
macro dG(A,fam,c1,c2) (fam*(1-c1*exp(-c2*A))) //first variation of surface energy density
macro ddG(A,fam,c1,c2) (fam*c1*c2*exp(-c2*A)) //second variation of surface energy density

//Mesh initialing and adaptation
int np=100; // starting mesh for adaptation
mesh Th = square(np, 10, [x*pi-pi*0.5, y/100]); //regular mesh
fespace SpaceP1(Th, P1);
SpaceP1 d = x < an1;
Th = adaptmesh(Th, d, hmax=hmaxval, hmin=hminval); // mesh adaptation

// Fespaces
fespace SpaceP0(Th, P0);
SpaceP0 k = k1*(x <= an1) + k2*(x > an1);
```

```
fespace Wh(Th, P1dc);
Wh f1, f2, f11, f12, f22, G1, G2, lam1,lam2;

fespace Vh(Th, [P1, P1]);
Vh [uu, vv]=[0,0], [w, s], [un, vn]=[l*cos(x),l*sin(x)];

fespace Sh(Th, P1);
Sh   u1,   v1;

// Equilibrium problem (vanishing of the first variation of the total energy)
varf vmass ([uu, vv], [w, s], solver=CG) = int2d(Th)(uu*w + vv*s);
matrix M = vmass(Vh, Vh);
problem NonLin([uu, vv], [w, s], solver=LU)
   =  int2d(Th, qforder=2)(k*cos(x)*(w*uu+s*vv)+f11*dl1(un, vn, uu, vv)*dl1(un, vn, w, s)*cos(x)
        +f12*dl1(un, vn, uu, vv)*dl2(w)
        +f12*dl1(un, vn, w, s)*dl2(uu)
        +f22*dl2(w)*dl2(uu)*1/cos(x)
        +f1*ddl1(un, vn, uu, vv, w, s)*cos(x)
        +G1*(ddl1(un,vn,uu,vv,w,s)*l2(un)+dl1(un,vn,w,s)*dl2(uu)+dl1(un,vn,uu,vv)*dl2(w))
        +G2*(dl1(un,vn,uu,vv)*l2(un)+l1(un,vn)*dl2(uu))*(dl1(un,vn,w,s)*l2(un)*1/cos(x)+l1(un,vn)*dl2(w)*1/
cos(x))
                                          )
                                          //
       -  int2d(Th, qforder=2)(
                                          Pa*ddV(un, vn, uu, vv, w, s))
   -int2d(Th, qforder=2)(
           (f1*dl1(un, vn, w, s)*cos(x)
               +f2*dl2(w)+k*cos(x)*((un-cos(x))*w+(vn-sin(x))*s))
               +G1*(dl1(un,vn,w,s)*l2(un)+l1(un,vn)*dl2(w))
          )
          + int2d(Th, qforder=2)(
          Pa*dV(un, vn, w, s)
          )
   +on(4, uu=0)+on(2, uu=0);

//  Newton's method
for (int i=0; i <100; i++){
   cout << "Loop " << i << endl;

   // Update
   f1 = df1(l1(un, vn),l2(un/(cos(x))), De, g);
   f2 = df2(l1(un, vn),l2(un/(cos(x))), De, g);
   f11=ddf11(l1(un, vn),l2(un/(cos(x))), De, g);
      f12=ddf12(l1(un, vn),l2(un/(cos(x))), De, g);
      f22=ddf22(l1(un, vn),l2(un/(cos(x))), De, g);
      G1=dG(l1(un, vn)*l2(un/(cos(x))),gam,d1,d2);
      G2=ddG(l1(un, vn)*l2(un/(cos(x))),gam,d1,d2);
      lam1=l1(un,vn);
      lam2=l2(un/(cos(x)));

   // Solve
   NonLin;
   w[]  = M*uu[];

   // Residual
   real res = sqrt(w[]' * uu[]); //L^2 norm of [uu, vv]
   cout << " L^2 residual = " << res << endl;

   // Update
   v1 = vv;
   u1 = uu;
   cout << "u1 min = " <<u1[].min << ", u1 max = " << u1[].max << endl;
   cout << "v1 min = " <<v1[].min << ", v1 max = " << v1[].max << endl;
   un[] -= uu[];

   if (res <1e-6) break;
} //end of Newton's cycle
```